

# Tomography of core-mantle boundary and lowermost mantle coupled by geodynamics

**Journal Article****Author(s):**

Soldati, Gaia; Boschi, Lapo; Forte, Alessandro M.

**Publication date:**

2012-05

**Permanent link:**

<https://doi.org/https://doi.org/10.3929/ethz-b-000048217>

**Rights / license:**

[In Copyright - Non-Commercial Use Permitted](#)

**Originally published in:**

Geophysical Journal International 189(2), <https://doi.org/10.1111/j.1365-246X.2012.05413.x>

# Tomography of core–mantle boundary and lowermost mantle coupled by geodynamics

Gaia Soldati,<sup>1</sup> Lapo Boschi<sup>2</sup> and Alessandro M. Forte<sup>3</sup>

<sup>1</sup>*Istituto Nazionale di Geofisica e Vulcanologia, Roma, Italy. E-mail: gaia.soldati@ingv.it*

<sup>2</sup>*Institute of Geophysics, E.T.H., Zürich, Switzerland*

<sup>3</sup>*GEOTOP, Université du Québec à Montréal, Canada*

Accepted 2012 February 7. Received 2012 January 7; in original form 2011 June 9

## SUMMARY

We propose an innovative approach to mapping CMB topography from seismic *P*-wave traveltimes inversions: instead of treating mantle velocity and CMB topography as independent parameters, as has been done so far, we account for their coupling by mantle flow, as formulated by Forte & Peltier. This approach rests on the assumption that *P* data are sufficiently sensitive to thermal heterogeneity, and that compositional heterogeneity, albeit important in localized regions of the mantle (e.g. within the *D'* region), is not sufficiently strong to govern the pattern of mantle-wide convection and hence the CMB topography. The resulting tomographic maps of CMB topography are physically sound, and they resolve the known discrepancy between images obtained from classic tomography on the basis of core-reflected and core-refracted seismic phases. Since the coefficients of mantle velocity structure are the only free parameters of the inversion, this joint tomography–geodynamics approach reduces the number of parameters; nevertheless the corresponding mantle models fit the seismic data as well as the purely seismic ones.

**Key words:** Inverse theory; Body waves; Seismic tomography; Dynamics of lithosphere and mantle.

## 1 INTRODUCTION

As noted early on by Morelli & Dziewonski (1987), the topography of the core–mantle boundary (CMB) is a key parameter to understand the nature of deep mantle flow and magnetic field generation, and an important factor to correct for if one is to image the structure of the Earth's core.

Seismologists have derived global maps of CMB topography based on compressional-wave traveltimes (e.g. Morelli & Dziewonski 1987; Rodgers & Wahr 1993; Obayashi & Fukao 1997; Boschi & Dziewonski 2000; Soldati *et al.* 2003) and the splitting of normal-mode eigenfrequencies (Ishii & Tromp 1999), to find only marginally consistent results. As Rodgers & Wahr (1993) first observed, the topography mapped on the basis of seismic phases reflected off the CMB (*PcP* phase) is not correlated with that derived from phases that are refracted through it (various branches of *PKP*). Boschi & Dziewonski (2000), Piersanti *et al.* (2001) and Soldati *et al.* (2003) show that the discrepancy between *PcP*- and *PKP*-based maps could be explained by the presence of relatively large heterogeneity in the fluid outer core, but fail to explain this unlikely feature. Fig. 6 of Ishii & Tromp (1999) shows that normal-mode based CMB topography is also not correlated with the results of traveltimes imaging.

Geodynamicists have predicted the topography of the CMB caused by mantle flow (Forte *et al.* 1995; Lassak *et al.* 2007, 2010).

Essentially, the CMB should be depressed under relatively dense and sinking regions of the lowermost mantle, and uplifted under less dense, rising ones. This effect can be modelled if a tomography model of seismic velocity in the mantle is interpreted in terms of equivalent density anomalies, a viscosity profile (typically based on observations of the geoid and/or postglacial rebound) is assumed, and the resulting flow is computed (e.g. Hager *et al.* 1985). Forte *et al.* (1995) found a good correlation between their geodynamical predictions and the seismic maps of CMB topography of Morelli & Dziewonski (1987). More recent studies suggest that the predictions of geodynamics are well correlated with *PcP*-based maps of CMB topography and not correlated at all with normal-mode- and *PKP*-based maps: compare, for example, fig. 1 of Soldati *et al.* (2003) and fig. 15 of Soldati *et al.* (2009). This discrepancy is partly solved if lateral heterogeneity is introduced in the outer core, but this feature lacks a clear physical explanation (Soldati *et al.* 2003).

Observations of Earth's rotation pole nutation have also been used to constrain indirectly the topography of the CMB. Nutations measured via Very Long Baseline Interferometry (VLBI) have been associated with the coupling between mantle and fluid core, with the ellipticity (i.e. the degree  $l = 2$ , order  $m = 0$  spherical harmonic component) of the CMB playing an important role. Gwinn *et al.* (1986) have explained VLBI data with an ellipticity of  $490 \pm 110$  m peak-to-valley. Their results have been confirmed

more recently by Buffett *et al.* (2002), although the amplitude of the excess ellipticity was estimated to be approximately 400 m.

All published global seismic maps of CMB topography so far have been derived by calculating the partial derivatives of seismic observations with respect to topography perturbations, which are then used to set up a linear inverse problem (Morelli & Dziewonski 1987; Rodgers & Wahr 1993; Obayashi & Fukao 1997; Ishii & Tromp 1999; Boschi & Dziewonski 2000; Soldati *et al.* 2003). This is based on some linearized equation relating seismic observations  $\delta s$  to mantle seismic velocity (and/or density)  $\delta v$  and CMB topography  $\delta c$ , that is,

$$\delta s = \int_V K_S(r, \theta, \phi) \delta v(r, \theta, \phi) dV + \int_\Omega K_C(\theta, \phi) \delta c(\theta, \phi) d\Omega, \quad (1)$$

where  $V$  denotes the volume of the Earth,  $\Omega$  the solid angle,  $K_S$  and  $K_C$  the velocity and CMB-topography partial derivatives (depending on the nature of the observation, and on the theoretical formulation of wave propagation/the Earth's free oscillations) and  $r, \theta, \phi$  are radius, colatitude and longitude, respectively. The left-hand side  $\delta s$  is an observation (traveltimes, normal-mode eigenfrequency . . .), while  $\delta v$  and  $\delta c$  are the unknown functions to be determined. Both  $\delta v$  and  $\delta c$  are then written as linear combinations of selected basis functions, and, in the presence of a large database of  $\delta s$ , a mixed-determined linear inverse problem (Menke 1989) is defined (e.g. Boschi & Dziewonski 1999).

With this study we propose an alternative approach, consisting of replacing  $\delta c$  in eq. (1) with an expression describing its dependence on  $\delta v$  through the physics of mantle convection. An analytical expression for  $\delta c$  in terms of  $\delta v$  is given, for example, by Forte *et al.* (1994), assuming (i) that mantle heterogeneity and the associated flow are of purely thermal origin (no compositional heterogeneity), so that density and velocity heterogeneity are proportional to one another, and (ii) that mantle viscosity is estimated reasonably well. The only unknown of the inverse problem is then the function  $\delta v$ , which is parameterized and inverted for as before. Although  $\delta c$  is not a free parameter of the inversion, the resulting models of  $\delta v$  implicitly account for the sensitivity of seismic data to  $\delta c$ .  $\delta c$  itself can be derived from  $\delta v$  after the inversion, using again the theory of Forte *et al.* (1994).

The neglect of compositional heterogeneity introduces a potential inaccuracy to our procedure, as a number of studies has indicated that the lowermost mantle is chemically heterogeneous (e.g. Karato 2003; Deschamps & Trampert 2003; Trampert *et al.* 2004; Della Mora *et al.* 2011). Our results should be seen as preliminary, before a way to account for compositional heterogeneity in our formulation is found. It is, however, not unlikely that the introduction of compositional heterogeneity will perturb only marginally the coupling between flow and CMB, and hence our models of the latter: it has been shown by Simmons *et al.* (2009), and earlier by Forte & Mitrović (2001), that even at the African superplume, where thermal and compositional heterogeneity have opposite effects on mantle flow, compositional effects are too weak to inhibit upward buoyancy forces.

In the following, we employ the geodynamical relationship between  $\delta c$  and  $\delta v$  in our implementation of the tomography inverse problem. Our goal is to employ our physical, *a priori* knowledge of the mantle-CMB system to reduce the non-uniqueness of tomography models.

## 2 SEISMOLOGY AND GEODYNAMICS BACKGROUND

### 2.1 Dynamic relationship between discontinuity topography and mantle density

If heterogeneities in the lower mantle are mainly thermal in origin, areas of high velocity can be associated to denser than average mantle, and low velocities to less dense mantle. With this assumption, analytical models of thermal convection can be developed (e.g. Hager *et al.* 1985; Forte & Peltier 1991), and a physical relationship between density heterogeneity and the undulation of global discontinuities in the Earth's interior can be established. In particular, Forte *et al.* (1994) showed that a simple relationship exists between perturbations in the density structure of the mantle  $\delta\rho$ , and the topography  $\delta c$  of the CMB, with  $\delta\rho$  and  $\delta c$  treated as small perturbations from a spherically symmetric reference model.

Let us introduce the spherical harmonic expansion of CMB topography

$$\delta c(\theta, \phi) = \sum_{l,m} \delta c_{lm} Y_{lm}(\theta, \phi), \quad (2)$$

where  $Y_{lm}$  is the spherical harmonic function of degree  $l$  and order  $m$ , and  $\delta c_{lm}$  is the corresponding spherical-harmonic coefficient of  $\delta c$ .

Eq. (5) of Forte *et al.* (1994) then stipulates that  $\delta c_{lm}$  are related to the  $r$ -dependent harmonic coefficients  $\delta\rho_{lm}$  of density perturbation through

$$\delta c_{lm} = \frac{1}{\Delta\rho_{cmb}} \int_c^a B_l(r) \delta\rho_{lm}(r) dr, \quad (3)$$

with  $c$  and  $a$  denoting the reference, mean radii of the CMB and Earth's surface, respectively, and  $\Delta\rho_{cmb} = -4.43 \text{ g cm}^{-3}$  the density jump across the CMB according to PREM (Dziewonski & Anderson 1981).

The 'kernels'  $B_l$  are  $l$ -dependent partial derivatives describing the response of CMB topography to density perturbations in the mantle. These kernels are calculated as explained by Forte & Peltier (1991), once the Earth's radial density and viscosity profiles are known. Constraining Earth's viscosity is subject to substantial uncertainties and non-uniqueness. We may neglect the effect of large-scale lateral viscosity variations (Moucha *et al.* 2007), and first compute  $B_l$  based on the viscosity profile of Mitrović & Forte (1997), shown to explain observations of both gravity and postglacial deformation; most of this study is based on this viscosity model. We next modify the profile of Mitrović & Forte (1997) to include a very low viscosity layer at the base of the mantle (Section 5.3), simulating the rheology of post-perovskite Yamazaki *et al.* (2006); Tosi *et al.* (2009); Ammann *et al.* (2010), expected to be the dominant phase in this depth range (D'' layer) (e.g. Murakami *et al.* 2004; Oganov & Ono 2004). In an additional set of experiments, we make use of the simpler model of Soldati *et al.* (2009) (Section 5.3). Fig. 1 includes all the viscosity profiles we experimented with.

Although the average density profile of the Earth is relatively well known (Dziewonski & Anderson 1981), lateral variations in density can in practice be estimated from those of seismic velocity. In establishing this scaling between seismic velocity and density anomalies, it is common to begin with the assumption that there are no lateral variations in the Earth's composition, nor pressure- or temperature-induced phase transformations; and in this case the velocity–density scaling may be estimated on the basis of laboratory measurements (e.g. Forte *et al.* 1994). This assumption of a

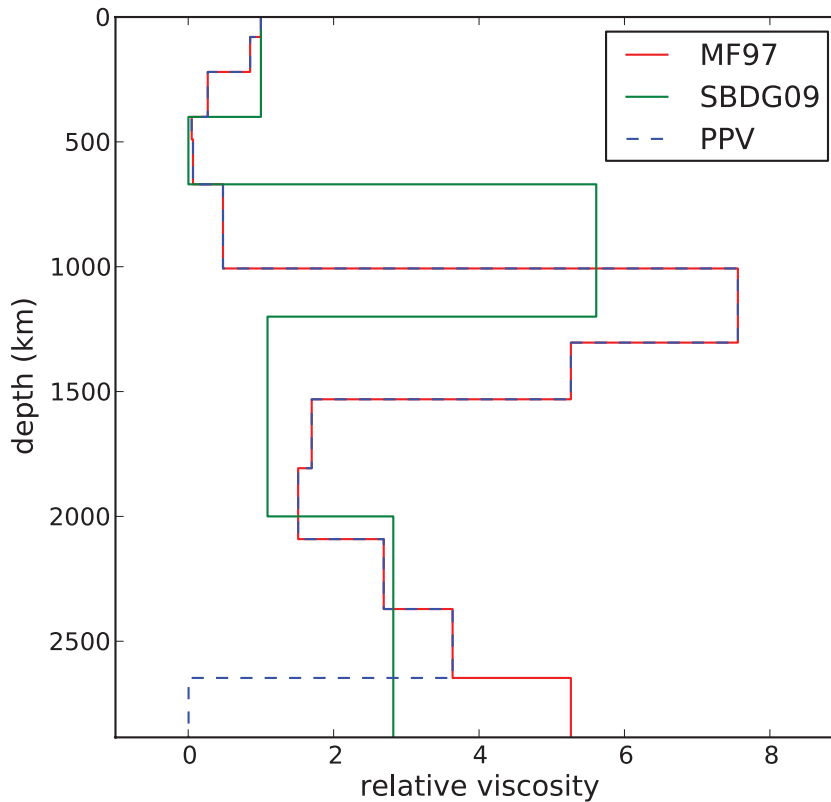


**Figure 1.** Viscosity models of the Earth used in this study, including: (solid red curve) the profile of Mitrovica & Forte (1997); (green) the one obtained by Soldati *et al.* (2009) inverting gravity and scaling density from the  $v_S$  model S20RTS (Ritsema *et al.* 1999, 2004); (blue) a profile we designed to simulate the effects of the perovskite to post-perovskite phase transition, replacing the model of Mitrovica & Forte (1997) in the bottom 250 km of the mantle with an extremely low-viscosity layer. Because flow modelling in this study only depends on viscosity ratios between different layers, each viscosity profile is normalized to its value in the shallowest layer.

depth-dependent velocity–density scaling has been relaxed in recent studies that allow for a fully 3-D relationship between seismic and density anomalies (Simmons *et al.* 2009, 2010). In this study, we simply assume that relative density anomalies are proportional to compressional-velocity ones, at all depths, through the constant factor  $\delta \ln \rho / \delta \ln v_p = 0.45$ , found by averaging the profile of Karato (1993). We repeated our experiment using a depth-dependent scaling in accordance with Karato & Karki (2001), and found that the resulting mantle and CMB models are only marginally affected. This is due to the relative weight of the seismic and geodynamic parts of the matrix to invert: the former is dominant for realistic values of the density–velocity scaling, and becomes comparable to the product of the geodynamic matrix by the scaling factor only for scalings one order of magnitude larger. For brevity we do not illustrate this test in detail.

We show in Fig. 2 (solid lines) the kernels  $B_l$  resulting, at several different harmonic degrees  $l$ , from the viscosity profile of Mitrovica & Forte (1997). Low- $l$  kernel values are non-negligible throughout the mantle, growing steadily from the Earth’s surface to the 660 km discontinuity and remaining constant down to the CMB. High- $l$  kernels are zero in the top 2000 km of the mantle, and grow quickly starting at a depth that itself grows with increasing  $l$ . The presence of a low-viscosity, post-perovskite layer (dashed lines) results in an additional quick growth of low-degree  $B_l$  with depth at the base of the mantle; the depth-dependence of high-degree  $B_l$  is more similar to that found from the viscosity model of Mitrovica & Forte (1997), except that their growth is confined to larger depths.

## 2.2 Mapping between spherical-harmonic and pixel parameterizations

In this study, we adhere to the approximately equal-area voxel parametrization of Boschi & Dziewonski (1999), Boschi & Dziewonski (2000) and Soldati *et al.* (2003). To make use of the results of Forte *et al.* (1994) in a voxel formulation, we need an operator that converts spherical-harmonic to pixel coefficients of a given function.

We define the characteristic function  $p_i(\theta, \phi)$  of the  $i$ th surface pixel in our grid,

$$p_i(\theta, \phi) = \begin{cases} 1 & \text{if } (\theta, \phi) \text{ lies within the } i\text{th pixel} \\ 0 & \text{elsewhere.} \end{cases} \quad (4)$$

A horizontal cross-section through a voxel-parametrized tomographic model of relative seismic velocity perturbation  $\delta v/v(r, \theta, \phi)$  can be thought of as a linear combination of pixel functions

$$\frac{\delta v}{v}(r, \theta, \phi) = \sum_i x_i(r) p_i(\theta, \phi) \quad (5)$$

through the  $r$ -dependent coefficients  $x_i(r)$ .

Provided that spherical harmonic coefficients are computed up to a sufficiently high  $l$ , one can accurately describe  $p_i(\theta, \phi)$  as a linear combination of spherical harmonics: we denote  $p_{i,lm}$  the coefficient of degree  $l$  and order  $m$  of the  $i$ th pixel function, so that

$$p_i(\theta, \phi) = \sum_{l,m} p_{i,lm} Y_{lm}(\theta, \phi). \quad (6)$$

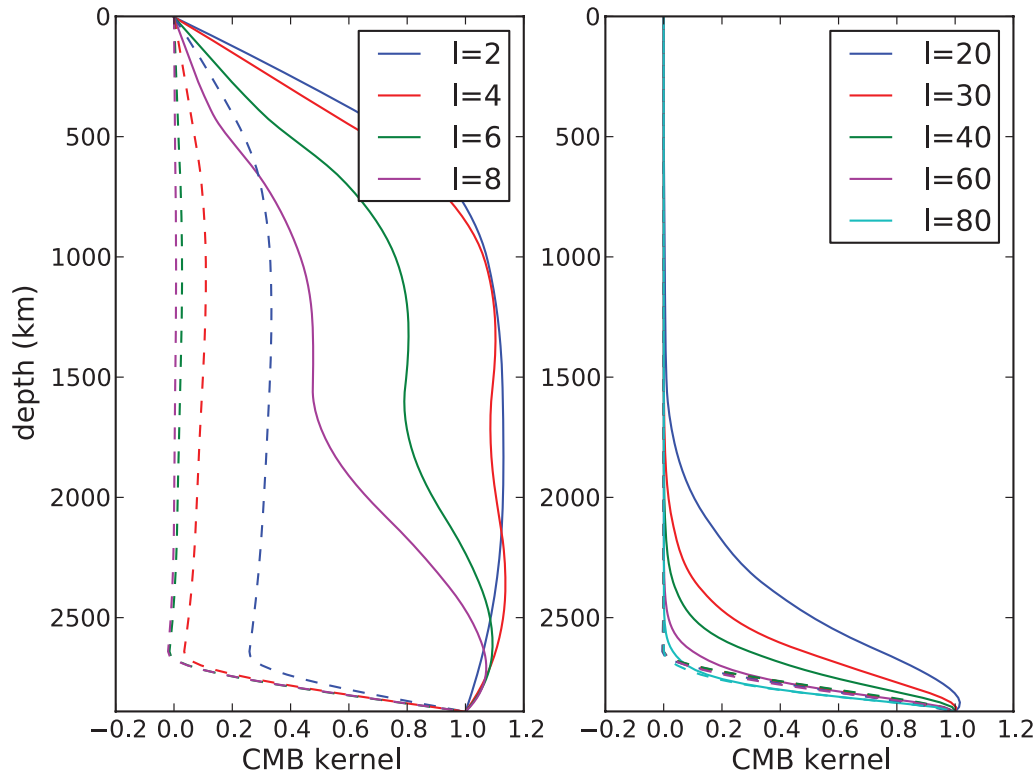


**Figure 2.**  $B_l$  kernels as a function of depth for (left-hand side) low harmonic degree  $l$  (colours as explained) and (right-hand side) relatively high  $l$ . Solid lines represent the CMB kernels based on the mantle viscosity profile of Mitrović & Forte (1997) (Fig. 1); dashed lines the ones obtained replacing the bottom 250 km of Mitrović & Forte (1997) viscosity model with a low-viscosity layer.

Let us now substitute eq. (6) into (5). We find

$$\frac{\delta v}{v}(r, \theta, \phi) = \sum_i x_i(r) \sum_{l,m} p_{i,lm} Y_{lm}(\theta, \phi), \quad (7)$$

and after changing the order of summation

$$\frac{\delta v}{v}(r, \theta, \phi) = \sum_{l,m} \left[ \sum_i x_i(r) p_{i,lm} \right] Y_{lm}(\theta, \phi). \quad (8)$$

We infer that pixel ( $x_i(r)$ ) and spherical-harmonic ( $x_{lm}(r)$ ) coefficients of  $\delta v/v$  are related by

$$x_{lm}(r) = \sum_i x_i(r) p_{i,lm}, \quad (9)$$

and the required operator simply consists of the harmonic coefficients of the pixel functions forming our parametrization grid. Depending on pixel size, the summation in eq. (6) will have to be extended to a different maximum degree  $l$ . Given the pixel size, we determine the maximum  $l$  by trial and error. Fig. 3 shows that, for the  $5^\circ \times 5^\circ$  parametrization used here (Section 3), all harmonic degrees up to  $l = 89$  must be considered.

### 2.3 Geodynamically self-consistent mantle/CMB tomography

Let us consider a spherically symmetric reference model  $v(r)$ ,  $c$  of  $P$ -wave velocity and CMB topography respectively, with laterally varying perturbations  $\delta v(r, \theta, \phi)/v(r)$  and  $\delta c(\theta, \phi)/c$ . The corresponding traveltime perturbation associated with a  $P$ -wave reflected by the CMB ( $PcP$  phase) can then be determined approximately through the linear equation (consistent with the general expression

(1) of Section 1)

$$\delta t = - \int_{\text{path}} \frac{\delta v(r(s), \theta(s), \phi(s))}{v^2(r)} ds + K_{pcp} \frac{\delta c(\theta_b, \phi_b)}{c} \quad (10)$$

(Boschi & Dziewonski 2000), where  $(\theta_b, \phi_b)$  are the coordinates at which the  $PcP$  raypath is reflected ('bounces') off the CMB,  $r = r(s)$ ,  $\theta = \theta(s)$ ,  $\phi = \phi(s)$  is the ray-path ('path') equation, and the sensitivity  $K_{pcp}$  of  $\delta t$  to CMB undulations depends on ray path geometry and is defined, for example, by Dziewonski & Gilbert (1976).

Although Boschi & Dziewonski (2000) and Soldati *et al.* (2003), among others, treat  $\delta c/c$  as a free parameter of their seismic inversions, we choose to rewrite it in terms of mantle  $\delta v/v$  through eq. (3) of Section 2.1. We replace  $\delta c$  in (10) with its spherical harmonic expansion (2),

$$\delta t = - \int_{\text{path}} \frac{\delta v}{v^2} ds + \frac{K_{pcp}}{c} \sum_{l,m} \delta c_{lm} Y_{lm}(\theta_b, \phi_b) \quad (11)$$

(where, in the interest of brevity, we have omitted the spatial-dependence of  $\delta v$  and  $v$ ), so that eq. (3) can be applied, and

$$\delta t = - \int_{\text{path}} \frac{\delta v}{v^2} ds + \frac{K_{pcp}}{c \Delta \rho_{cmb}} \sum_{l,m} \int_c^a B_l(r) \delta \rho_{lm}(r) dr Y_{lm}(\theta_b, \phi_b). \quad (12)$$

As discussed above, if we assume that compositional heterogeneity be relatively small (Schuberth *et al.* 2009; Simmons *et al.* 2010; Della Mora *et al.* 2011), a constant or spherically symmetric scaling factor  $\beta(r)$  can be introduced so that  $\delta \rho_{lm}/\rho(r) = \beta(r)x_{lm}(r)$ , with  $x_{lm}(r)$  the  $r$ -dependent harmonic coefficients of relative  $P$ -wave

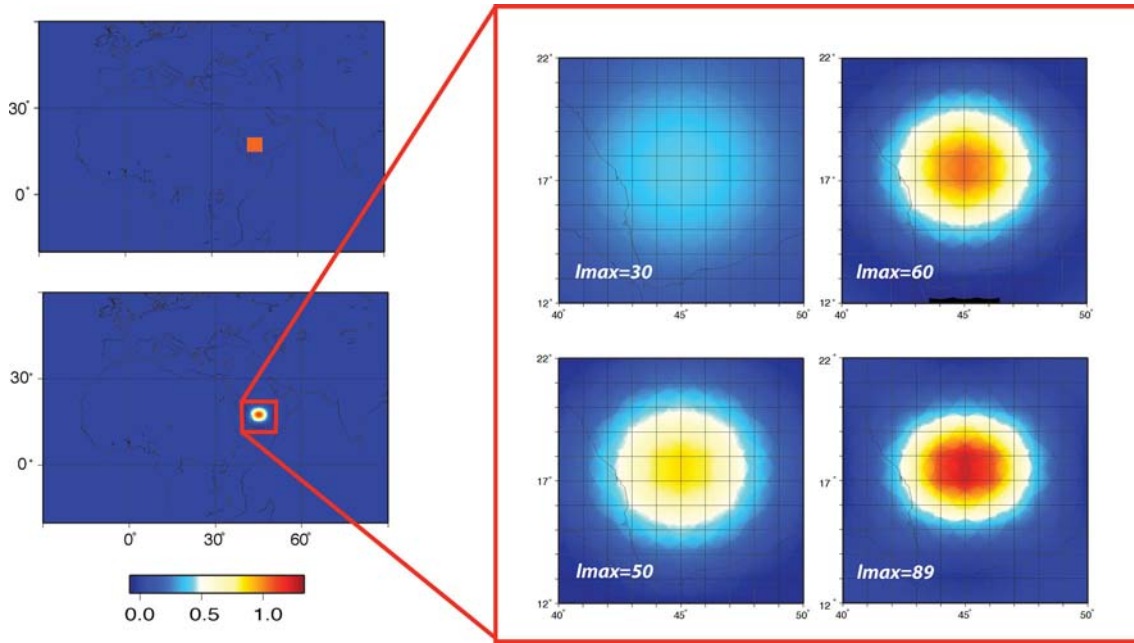


**Figure 3.** Left-hand side: The top grid, representing a single pixel (orange square) of area  $5^\circ \times 5^\circ$  and centred on the southern part of Arabian Peninsula ( $17.5^\circ \text{N}$ ,  $45^\circ \text{E}$ ) has been expanded in spherical harmonics and then transformed back to grid (bottom panel) summing over the harmonics to different harmonic degrees. Right-hand side: The comparison between the four plots shows that increasing the harmonic degree  $l$  the pixel is resolved better and better, and it is almost entirely reproduced for  $l_{\text{max}} = 89$ .

velocity heterogeneity  $\delta v/v(r, \theta, \phi)$ . Then

$$\delta t = - \int_{\text{path}} \frac{\delta v}{v^2} ds + \frac{K_{pcp}}{c \Delta \rho_{cmb}} \sum_{l,m} \int_c^a B_l(r) \beta(r) \rho(r) x_{lm}(r) dr Y_{lm}(\theta_b, \phi_b). \quad (13)$$

We now make use of the results of Section 2.2. Specifically, we replace  $x_{lm}(r)$  with its expression (9). Denoting  $R_k(r)$  the basis functions used to describe the  $r$ -dependence of  $\delta v$ , so that  $x_i(r) = \sum_k x_{ik} R_k(r)$ , eq. (9) takes the form

$$x_{lm}(r) = \sum_{i,k} x_{ik} p_{i,lm} R_k(r), \quad (14)$$

and substituting into (13),

$$\delta t = - \int_{\text{path}} \frac{\delta v}{v^2} ds + \frac{K_{pcp}}{c \Delta \rho_{cmb}} \sum_{l,m} \int_c^a B_l(r) \beta(r) \rho(r) \sum_{i,k} x_{ik} p_{i,lm} R_k(r) dr Y_{lm}(\theta_b, \phi_b). \quad (15)$$

In practice, we choose the  $R_k(r)$  to be a set of non-overlapping adjacent layers spanning the entire mantle; in analogy with Boschi & Dziewonski (1999), Boschi & Dziewonski (2000) and Soldati *et al.* (2003), the product  $R_k(r)p_i(\theta, \phi)$  then defines a voxel.

$\delta v/v$  can be written as a linear combination of voxels,

$$\delta v/v = \sum_{i,k} x_{ik} p_i(\theta, \phi) R_k(r). \quad (16)$$

Replacing  $\delta v/v$  in the first term at the right-hand side of (15) with its expression (16),

$$\delta t = - \int_{\text{path}} \frac{1}{v} \sum_{i,k} x_{ik} p_i(\theta, \phi) R_k(r) ds + \frac{K_{pcp}}{c \Delta \rho_{cmb}} \sum_{l,m} \int_c^a B_l(r) \beta(r) \rho(r) \sum_{i,k} x_{ik} p_{i,lm} R_k(r) dr Y_{lm}(\theta_b, \phi_b). \quad (17)$$

After changing the order of summation,

$$\delta t = \sum_{i,k} x_{ik} \left[ - \int_{\text{path}} \frac{1}{v} p_i(\theta, \phi) R_k(r) ds + \frac{K_{pcp}}{c \Delta \rho_{cmb}} \sum_{l,m} p_{i,lm} \int_c^a B_l(r) \beta(r) \rho(r) R_k(r) dr Y_{lm}(\theta_b, \phi_b) \right]. \quad (18)$$

The expression in square brackets at the right-hand side of eq. (18) can be computed for any *PcP* ray path once a reference Earth model ( $\rho(r)$ ,  $v(r)$ ,  $\beta(r)$ ,  $\Delta \rho_{cmb}$ ) and a voxel grid ( $p_i(\theta, \phi)$ ,  $R_k(r)$ ) are defined. If eq. (18) is implemented for each observation of *PcP* traveltimes in our database, and an index  $j$  is assigned to the resulting equations, one can denote  $A_{j,ik}$  the term within square brackets in (18), and

$$\delta t_j = \sum_{i,k} A_{j,ik} x_{ik}, \quad (19)$$

which is typically a large, mixed-determined linear system (Menke 1989). Eq. (19) is analogous to eq. (7) of Boschi & Dziewonski (1999), and can be solved by least-squares methods in exactly the same way. The coefficients  $x_{ik}$  describing mantle  $\delta v/v$ , and CMB topography are not free parameters in the inversion.

In the case of seismic phases refracted through the CMB, for example, *PKP*, the above treatment can be repeated after replacing eq. (10) with

$$\delta t = - \int_{\text{path}} \frac{\delta v(r(s), \theta(s), \phi(s))}{v^2(r)} ds + K_{pkp}^{\text{in}} \frac{\delta c(\theta_{\text{in}}, \phi_{\text{in}})}{c} + K_{pkp}^{\text{out}} \frac{\delta c(\theta_{\text{out}}, \phi_{\text{out}})}{c}, \quad (20)$$

where  $(\theta_{\text{in}}, \phi_{\text{in}})$  and  $(\theta_{\text{out}}, \phi_{\text{out}})$  denote the coordinates of the ray path's entry and exit points at the CMB. The sensitivity  $K_{pkp}^{\text{in}}$  and  $K_{pkp}^{\text{out}}$  of the *PKP* traveltimes to CMB topography depends, again, on the ray path incidence angle at the CMB (e.g. Dziewonski & Gilbert 1976).

## 2.4 Tomographic and geodynamically constrained inversions

The treatment of Section 2.3 should be compared with that of Boschi & Dziewonski (2000), who simply replace  $\delta v/v$  in eq. (10) with its voxel expansion (16) and  $\delta c/c$  with an analogous, pixel expansion  $\delta c/c = \sum_i c_i p_i(\theta, \phi)$ . From the resulting equation they derive a linear system of the form (19), where the unknown values of CMB topography  $c_i$  are, together with velocity perturbations, entries of the unknown vector at the right-hand side. As opposed to the method described in Section 2.3, there is no guarantee that the CMB topography of models obtained in this way be consistent with what expected from the corresponding mantle model on the basis of geodynamics.

In the following, we shall alternatively apply the tomography approach of Boschi & Dziewonski (2000) (resulting in ‘ $T$ ’ models) and the joint tomography–geodynamics approach of Section 2.3 above (‘ $TG$ ’ models).

## 3 SEISMIC DATA, TOMOGRAPHIC PARAMETERIZATION AND REGULARIZATION

Our tomographic inversions are all derived from the database of Antolik *et al.* (2001), including  $P$ ,  $PKPbc$ ,  $PKPdf$  and  $PcP$  traveltimes corrected from the International Seismological Centre (ISC) bulletin. Exactly the same database was employed by Soldati *et al.* (2003). This database is preferable to the updated bulletin of Engdahl *et al.* (1998), in that hypocentres were further relocated (and traveltimes accordingly corrected) to account for 3-D mantle structure and the crustal model Crust5.1 of Mooney *et al.* (1998). (In recent years the global earthquake and station distribution remained essentially unchanged.) The contribution of crustal structure to traveltimes is also estimated on the basis of Crust5.1, and subtracted from the data, such that the residual traveltimes should then be approximately sensitive only to the mantle. The observations (several millions) of Antolik *et al.* (2001) are combined to form summary-ray traveltimes:  $\sim 70\,000$   $PcP$ ,  $\sim 30\,000$   $PKPbc$ ,  $\sim 150\,000$   $PKPdf$ ,  $\sim 630\,000P$ . Following Boschi & Dziewonski (2000) and Soldati *et al.* (2003), we neglect the more noisy  $ab$  branch of  $PKP$ . In the following, we shall jointly invert various combinations of the  $P$ ,  $PcP$  and  $PKP$  databases, investigating whether different phases provide consistent maps of the CMB.  $P$  data serve to constrain mantle structure as robustly as possible, limiting the amount of smearing of unresolved mantle heterogeneity into the CMB maps (e.g. Boschi & Dziewonski 2000).

We follow Soldati *et al.* (2003) also in their choice of parametrization, consisting of 15 equal-thickness ( $\sim 200$  km) layers each subdivided into 1656 voxels of approximately equal horizontal extent ( $5^\circ \times 5^\circ$  at the equator). Our  $TG$  models then consist of 24 840 free parameters.  $T$  models include 1656 additional pixels describing the CMB topography, resulting in 26 496 free parameters total. All inversions are regularized, requiring that the roughness of both  $\delta v_p$  and  $\delta c$ , as implemented by Boschi & Dziewonski (1999) for voxel/pixel parametrizations, be minimum. Consistently with Soldati *et al.* (2003), the norm of  $\delta c$  (not of  $\delta v_p$ ) is also damped. Independent regularization weights (‘damping parameters’) for  $\delta v_p$  and  $\delta c$  are selected based on the synthetic tests described in Section 4 described later (input and output models should be as similar as possible), while also verifying that our new models are globally consistent with earlier, independent results (e.g. Becker & Boschi 2002; Boschi *et al.* 2007, 2008). For consistency, we applied to the

inversions of synthetic and real data, and to  $T$  and  $TG$  inversions, the exact same regularization weights.

We assume PREM to be exactly valid within the outer core, but correct  $PKPdf$  traveltimes for inner-core anisotropy according to the model of Su & Dziewonski (1995). As mentioned by Boschi & Dziewonski (2000), whether or not the latter correction is applied has little effect on mapped mantle and CMB structure.

## 4 SYNTHETIC TESTS

A synthetic test consists of (i) selecting an arbitrary, ‘input’ model of mantle and CMB structure; (ii) computing input-model theoretical traveltimes for all summary source–station couples in our database, and for all observed phases ( $P$ ,  $PcP$ ,  $PKP$ ); (iii) substituting  $\delta t_j$  with those theoretical traveltimes in eq. (19), and least-squares solving. The similarity of the resulting ‘output’ model to the input is a measure of data and algorithm resolution (e.g. Boschi 2003).

We compute two different sets of synthetic data, each associated with a different input model, and in both cases invert them with both the  $T$  and  $TG$  approaches: this allows us to evaluate the relative performance of our new, joint seismic–geodynamic method with respect to classical tomography. Both input models are by construction geodynamically self-consistent, that is, the input CMB topography is computed, through eq. (3), from the assumed mantle  $v_p$  model, based on the viscosity profile of Mitrovica & Forte (1997) and on our assumed scaling factor  $\delta \ln \rho / \delta \ln v_p$ .

Gaussian random noise is added to the synthetic data, with variance selected as half the variance of each data set, namely 0.8 s for direct  $P$  traveltimes, 0.7 s for  $PKPbc$ , 1.3 s for  $PKPdf$  and 1.9 s for  $PcP$ .

### 4.1 Checkerboard test

We first compute traveltime synthetics based on the ‘checkerboard’ input model shown in Fig. 4 (left column), coinciding with the  $l = 8$ ,  $m = 4$  spherical harmonic function with amplitude  $\delta v_p/v_p = 1.5$  per cent and a change of sign (not of pattern) every 400 km radially (two layers). As anticipated, the input CMB model is not defined arbitrarily, but derived from the input  $\delta v_p/v_p$  through eq. (3): this results in a checkerboard-like topography perfectly anticorrelated (negative topography under fast, cold, dense mantle) with the velocity heterogeneity of the immediately overlying, lowermost-mantle layers (Section 1).

From this model, we compute synthetic traveltimes associated with recorded  $P$  and  $PcP$  arrivals. We then invert them jointly, first with the  $T$  and then with the  $TG$  approach. In the  $TG$  case, the output CMB is of course not part of the least squares solution, but computed from the output mantle via eq. (3).

The results of both experiments are illustrated in the middle and right columns of Fig. 4. The  $T$  and  $TG$  methods are equally successful (or unsuccessful) in reproducing the input pattern within the mantle. In both cases, good tomography resolution is limited to areas that are covered well by the data (compare, e.g. with fig. 2 of Soldati & Boschi (2005)). Both output models are characterized by an evident loss in amplitude of  $\delta v_p/v_p$  with respect to the input. More interestingly, the CMB topography is only recovered by the  $TG$  inversion. For such a complex input model (many changes of sign in the vertical direction within the mantle, and relatively short-wavelength CMB topography), the geographic coverage of  $PcP$  is apparently too poor, and at many locations the output model is actually anticorrelated with the input.

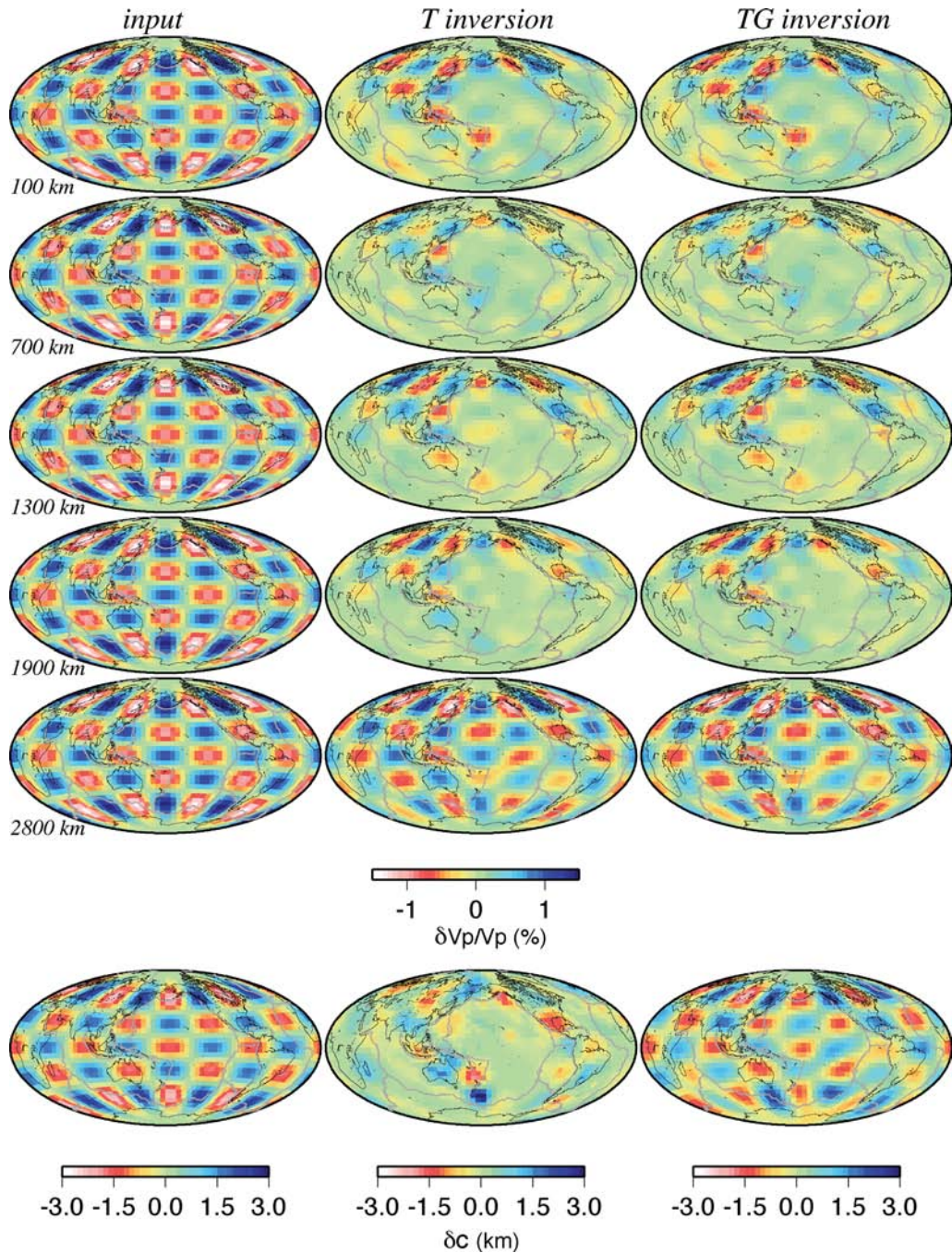


**Figure 4.** Result of a checkerboard test: input model (left hand side), output  $P + PcP$ -derived seismic model (middle panel), output  $P + PcP$ -derived seismic-geodynamic model (right hand side). Relative velocity heterogeneities (top panel) range between  $-1.5$  percent and  $1.5$  percent, CMB topography (bottom panel) between  $-3$  and  $+3$  km.

We repeat this exercise with the same input model for the combined  $P$  and  $PKP_{df}$  data set, and the results are shown in Fig. 5. Similar conclusions as above can be drawn, with the important difference that  $PKP_{df}$  data can resolve both mantle anomalies and CMB topography also via the  $T$  approach.  $TG$  yet clearly outperforms  $T$ : the amplitude of output CMB undulations is comparable with the input, and a consistent pattern of undulations is reproduced over a much wider area.

The rms of the difference between input and output model at each model voxel/pixel (Table 1), and the correlation between input and output model (Table 2) confirms that  $TG$  output models are closer

to the input than  $T$  ones. Inversions of  $PcP$  or  $PKP_{df}$  (along with  $P$ ) synthetic traveltimes are equally successful in reproducing the input mantle, whether the  $TG$  or  $T$  approach is used; but, in the assumption that heterogeneity be of purely thermal origin, the  $TG$  approach is systematically better at resolving CMB topography.

#### 4.2 Recovery test

We next select as input a ‘realistic’ model of mantle  $v_p$  heterogeneity (obtained by inverting the joint direct  $P$  and  $PcP$  data set for mantle  $\delta v_p/v_p$  and CMB topography, and shown in

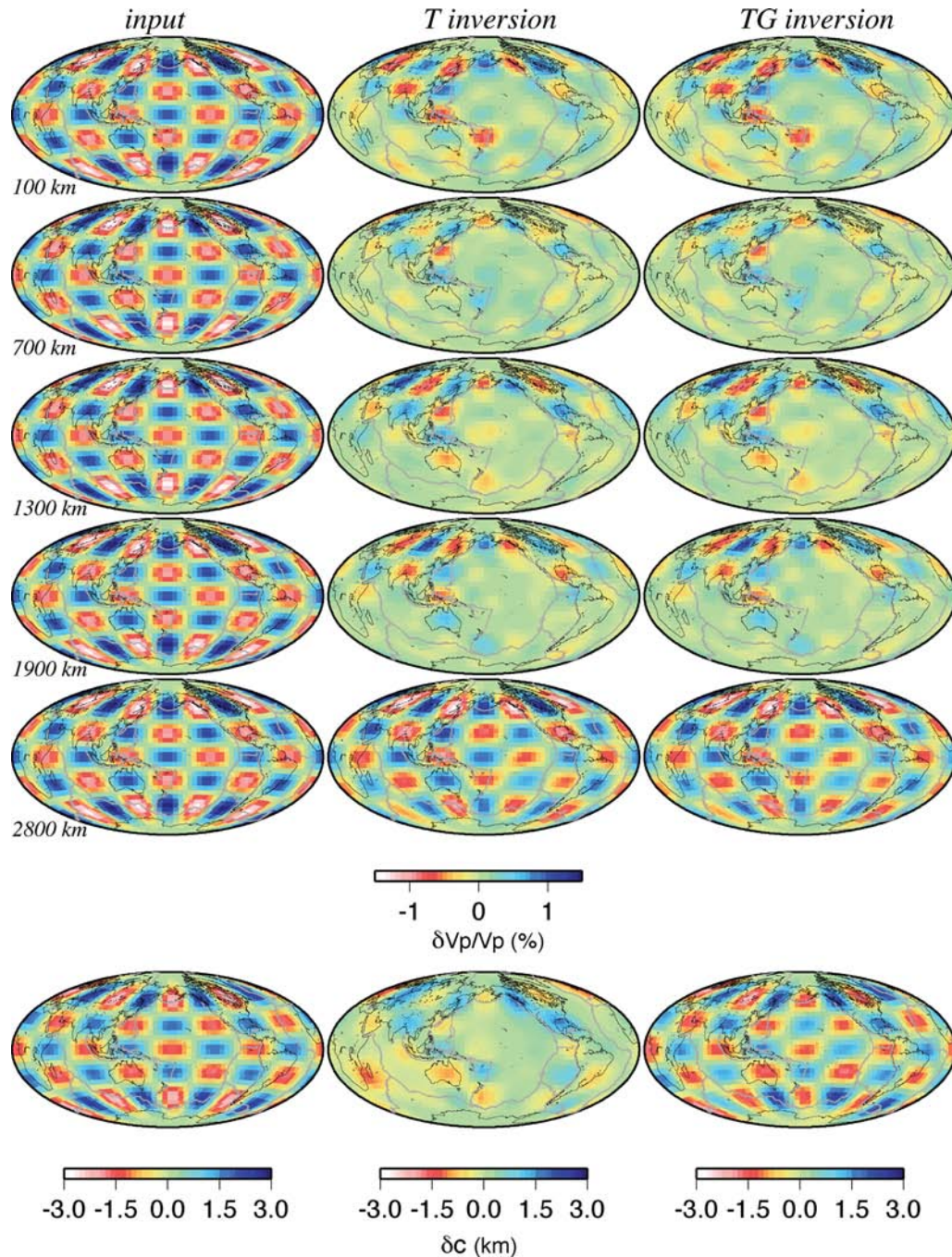


**Figure 5.** Same as previous figure, with output models obtained inverting  $P+PKPdf$  data. All models include mantle velocity heterogeneities (per cent) and CMB topography (km).

Fig. 6, left column), use, again, eq. (3) to compute the associated CMB topography, and compute, noise and invert the associated synthetic data as described in Section 4.1. We summarize the results in Figs 6 and 7, corresponding to inversions of the combined  $P$  and  $PcP$ , and combined  $P$  and  $PKPdf$  data sets, respectively.

Velocity anomalies in the mantle are reproduced well in both  $T$  and  $TG$  output models, with amplitudes only slightly weaker than the input ones in the lowermost mantle of the  $T$  model. The CMB is recovered almost perfectly by our  $TG$  inversions;  $T$  inversions of both  $PcP$  and  $PKPdf$  data lead to quite different output CMB maps, although both at least partially consistent with the input.

Again, we compute difference rms and correlation between output and input models in the various cases, and summarize them in Tables 3 and 4, respectively. The performance of the two methods is comparable as far as only mantle structure is concerned, but the  $TG$  method outperforms the  $T$  one in resolving CMB topography.

## 5 APPLICATION TO THE ISC DATABASE

### 5.1 Geodynamically self-consistent tomographic images

To correctly evaluate the difference between classic tomographic inversions ( $T$ ) and seismic/geodynamic results ( $TG$ ), one must make

**Table 1.** Checkerboard test: rms of the difference between input and output models, computed from the entire mantle (MAN), the two lowermost mantle layers (LMM), and the CMB topography (CMB). These values are obtained from independent  $T$  and  $TG$  inversions of either the combined  $P$  and  $PKP_{df}$ , or  $P$  and  $PcP$  data sets, as indicated in the first column.

Inverted data	MAN	LMM	CMB
$P + PcP (T)$	0.479	0.245	1.192
$P + PcP (TG)$	0.478	0.234	0.4181
$P + PKP_{df} (T)$	0.477	0.200	0.813
$P + PKP_{df} (TG)$	0.477	0.207	0.279

**Table 2.** Checkerboard test: correlation between input and output models (acronyms same as Table 1).

Inverted data	MAN	LMM	CMB
$P + PcP (T)$	0.680	0.943	-0.168
$P + PcP (TG)$	0.683	0.944	0.919
$P + PKP_{df} (T)$	0.685	0.960	0.627
$P + PKP_{df} (TG)$	0.683	0.961	0.966

sure to follow the same procedure in the two cases, and that the mantle models be equivalently regularized. As for the CMB topography, the damping applied to the  $T$  inversions has no counterpart in the  $TG$  method, where the CMB is obtained by integration of mantle velocity heterogeneity rather than by inversion of traveltimes.

Similar to Section 4 and to Soldati *et al.* (2003), we first conduct independent  $T$  inversions of different combinations of the  $P$ ,  $PcP$ ,  $PKP_{df}$  and  $PKP_{bc}$  traveltime data sets. The results, obtained with the same regularization scheme and weights as the synthetic tests in Section 4, are shown in Fig. 8. Direct  $P$  traveltimes are always included in the inverted database to guarantee that mantle structure is constrained as robustly as possible: trade-off between mantle and CMB structure is thus minimized. Following Boschi & Dziewonski (1999) and Boschi & Dziewonski (2000), data are weighted before inversion according to the extent to which each traveltime deviates from PREM predictions; the weight  $w_j$  of the datum  $\delta t_j$  is an exponential function whose argument is proportional to the difference between observed and reference traveltime:

$$w_j = e^{(\delta t_{\text{ref}} - |\delta t_j|)}. \quad (21)$$

The mantle  $v_p$  heterogeneity models derived with different subsets of data essentially agree with each other and with previously published ones (e.g. Boschi & Dziewonski 1999, 2000), except for minor differences in the lowermost mantle, likely reflecting the non-uniformity of data coverage: fictitious structure may be mapped in regions that are sampled relatively sparsely by seismic rays. Most importantly, the  $T$  inversion of the combined  $P$  and  $PcP$  data set results in a CMB map that is inconsistent with the  $P$  and  $PKP_{df, bc}$  ones:  $PcP$ -derived CMB topography is characterized by a  $C$ -shaped depression under Eastern Asia, Kamchatka peninsula and the Americas, while the  $PKP$  maps are dominated by a major topographic high under Southeastern Asia. A similar discrepancy has been observed in previous studies (e.g. Rodgers & Wahr 1993); since all the regions in question are sampled well by the data, lack of tomography resolution cannot, alone, account for it. The discrepancy has been shown to be reduced when assuming a laterally heterogeneous outer core, consistent with the results of some independent studies (e.g. Ritzwoller *et al.* 1986), but the latter scenario still lacks a

physical explanation (Boschi & Dziewonski 2000; Piersanti *et al.* 2001; Soldati *et al.* 2003).

We repeat all inversions with our new  $TG$  method described in Section 2.3, to find the solution models shown in Fig. 9. CMB topography is computed a posteriori from the mantle solution. The significant discrepancy between  $PcP$ - and  $PKP$ -based models of Fig. 8 disappears in the new maps of CMB topography, characterized by (i) depression along the Pacific rim, possibly associated with deep subducting plates, and (ii) elevation under the large, lowermost-mantle low shear velocity provinces under central Pacific and south/west Africa. This pattern is consistent with the discussion of Section 2.1.

An important metric of model quality is variance reduction. After each  $T$  or  $TG$  inversion, we calculate how much the solution model reduces the variance of each individual data set ( $P$ ,  $PcP$ ,  $PKP_{df, bc}$ ). We first calculate variance reduction of data weighted as described earlier. The results are shown in Fig. 10. There is a slight but systematic decrease in the variance reduction achieved with  $TG$  with respect to  $T$  inversions. This is not surprising, as the  $TG$  method involves a decrease in the number of free parameters (model coefficients) available to fit the data: the 1656 CMB topography pixels that are now coupled with mantle  $v_p$  voxels. We next calculate variance reduction of raw, non-weighted data, and find that the value achieved by  $TG$  models is higher for all phases (Fig. 11): the effect seen in Fig. 10 is reversed. Our  $TG$  models explain better than  $T$  models data that were not, or not entirely accounted for in both  $T$  and  $TG$  inversions. This improvement in data fit cannot be explained by tomographic artefacts as it corresponds to a decrease in the number of free parameters, and we infer that it might reflect an effective enhancement of model quality (Menke 1989; Tarantola 2005).

We compare the  $T$  and  $TG$  models quantitatively using the same metrics of Section 4, that is, model correlation and rms difference. We compute their values over the entire mantle, over the bottom two lowermost-mantle layers, and over the CMB topography only. The results are shown in Fig. 12.  $T$  and  $TG$  images of the mantle as a whole are very similar; maps of the lowermost mantle alone are slightly less well correlated than average (rms difference is also slightly stronger); discrepancies in  $T$  and  $TG$  maps of CMB topography are comparably large.

## 5.2 Comparison with independent $v_p$ and $v_s$ tomography models

To understand whether our  $TG$  models of  $v_p$  velocity introduce some change in the ratio  $v_s/v_p$  compared to the purely tomographic models  $T$ , and consequently a different interpretation of mantle structure/composition, we calculate the correlation of the  $T$  and  $TG$  models derived here from the entire  $P$ ,  $PcP$ ,  $PKP$  database, with the  $PMEAN$  and  $SMEAN$  models of Becker & Boschi (2002). The results are shown in Fig. 13 in the same style as analogous figures in Becker & Boschi (2002). Being obtained from the combination of different earlier models, each particularly robust over a different depth range,  $PMEAN$  and  $SMEAN$  are a reasonable choice of ‘reference’ models.  $SMEAN$  in particular has been shown to fit broadband seismic data at least as well (Qin *et al.* 2008), and geoid observations better (Steinberger & Antretter 2006) than other recent tomographic models.

Figs 13(a) and (c) show that the correlation between  $PMEAN$  and both our  $T$  and  $TG$  models is very high over most of the mantle. This is not surprising given that  $PMEAN$  was derived from essentially the same data as our models. In the lowermost mantle, where

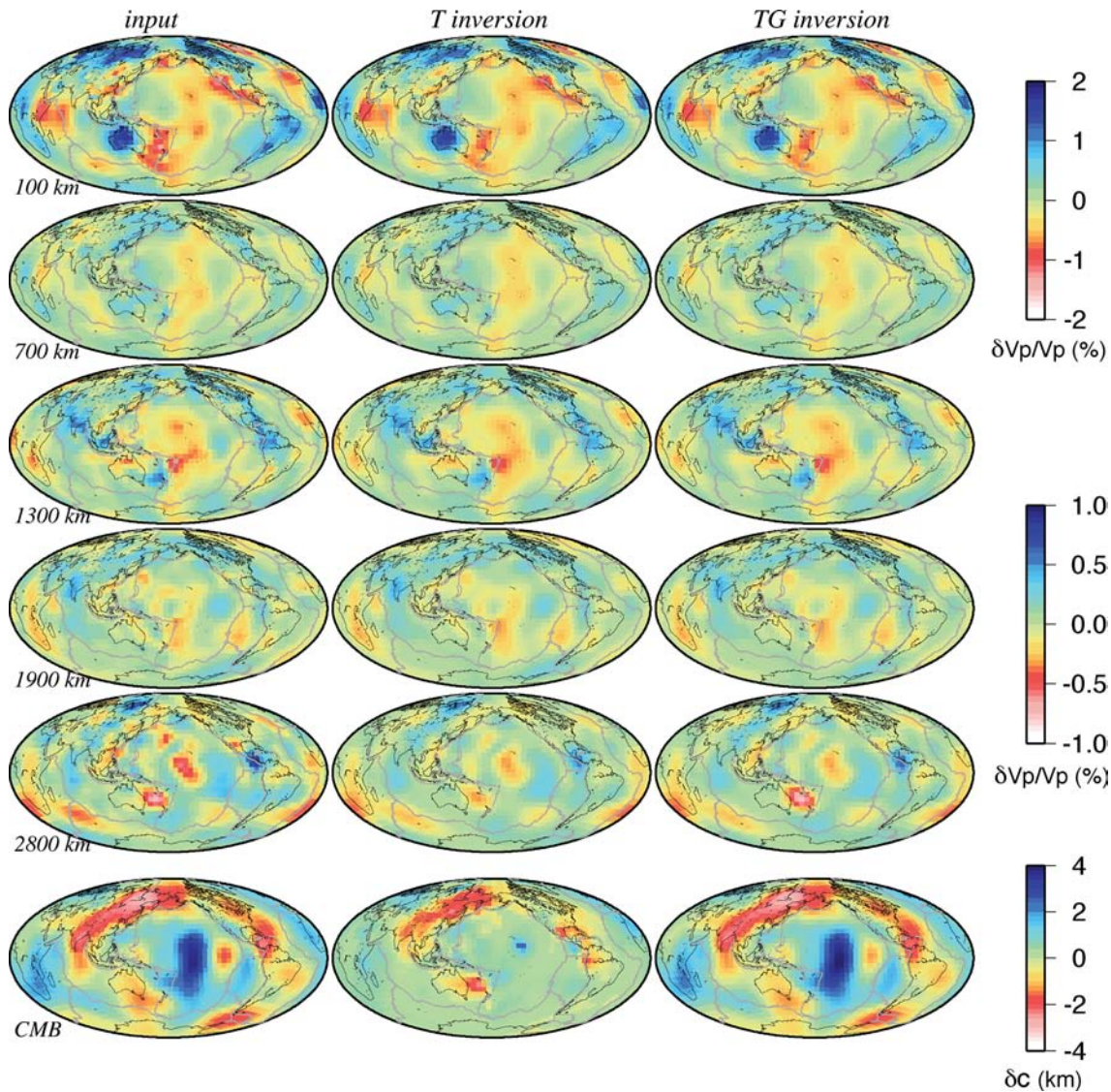


**Figure 6.** Result of a recovery test: input model (left-hand side), output  $P + PcP$ -derived seismic model (middle panel), output  $P + PcP$ -derived seismic-geodynamic model (right-hand side). All models include mantle velocity heterogeneities (per cent) and CMB topography (km).

the latter are also based on  $PKP$  and  $PcP$  data, not accounted for by  $PMEAN$ , the correlation is lower. Correlation between  $SMEAN$  and our models (Figs 13b, d) is much lower than that of  $PMEAN$ , confirming the differences between  $v_s$  and  $v_p$  patterns at relatively high harmonic degrees throughout the mantle, and particularly in the lowermost mantle (Della Mora *et al.* 2011). Together with the anomalously high ratio of  $v_s$  to  $v_p$  anomaly, this decorrelation has been interpreted as being caused by chemical, rather than purely thermal heterogeneity (e.g. Ishii & Tromp 1999; Forte & Mitrova 2001; Trampert *et al.* 2004). In this context, it is interesting to note that  $v_p$  anomaly amplitudes from  $TG$  models are systematically, albeit only slightly higher than those of  $T$  models, although the correlation between  $T$  and  $PMEAN/SMEAN$  models is essentially as high as that between  $TG$  and  $PMEAN/SMEAN$ .

### 5.3 A very low viscosity, post-perovskite layer in the lowermost mantle

Results discussed so far were obtained assuming the radial mantle viscosity profile of Mitrova & Forte (1997) (Fig. 1). We have

repeated our experiments with alternative viscosity profiles, for example, that of Soldati *et al.* (2009) (also shown in Fig. 1), and we calculated the fit to geodynamical and seismic data. The results are similar to those of Section 5.1 and we do not show them here in the interest of brevity.

Gravity and postglacial rebound data used to constrain mantle viscosity are approximately insensitive to lowermost mantle rheology (Soldati *et al.* 2009). However, it has been recently shown that mantle materials undergo a phase transition from perovskite to post-perovskite (Murakami *et al.* 2004; Oganov & Ono 2004), presumably associated with the  $D'$  seismic layer in the lowermost mantle. Several studies have also shown post-perovskite to be characterized by higher density and, perhaps, orders-of-magnitude lower viscosity than post-perovskite (Yamazaki *et al.* 2006; Tosi *et al.* 2009; Ammann *et al.* 2010). A broad lowermost-mantle layer of anomalously low viscosity is likely to affect strongly deep mantle flow, and, subsequently, the mantle–CMB kernels of Section 2.1. As anticipated in Section 2.1, we model this effect correcting the bottom 250 km of the viscosity profile assumed so far (Mitrova & Forte 1997), where we now impose a viscosity  $10^3$

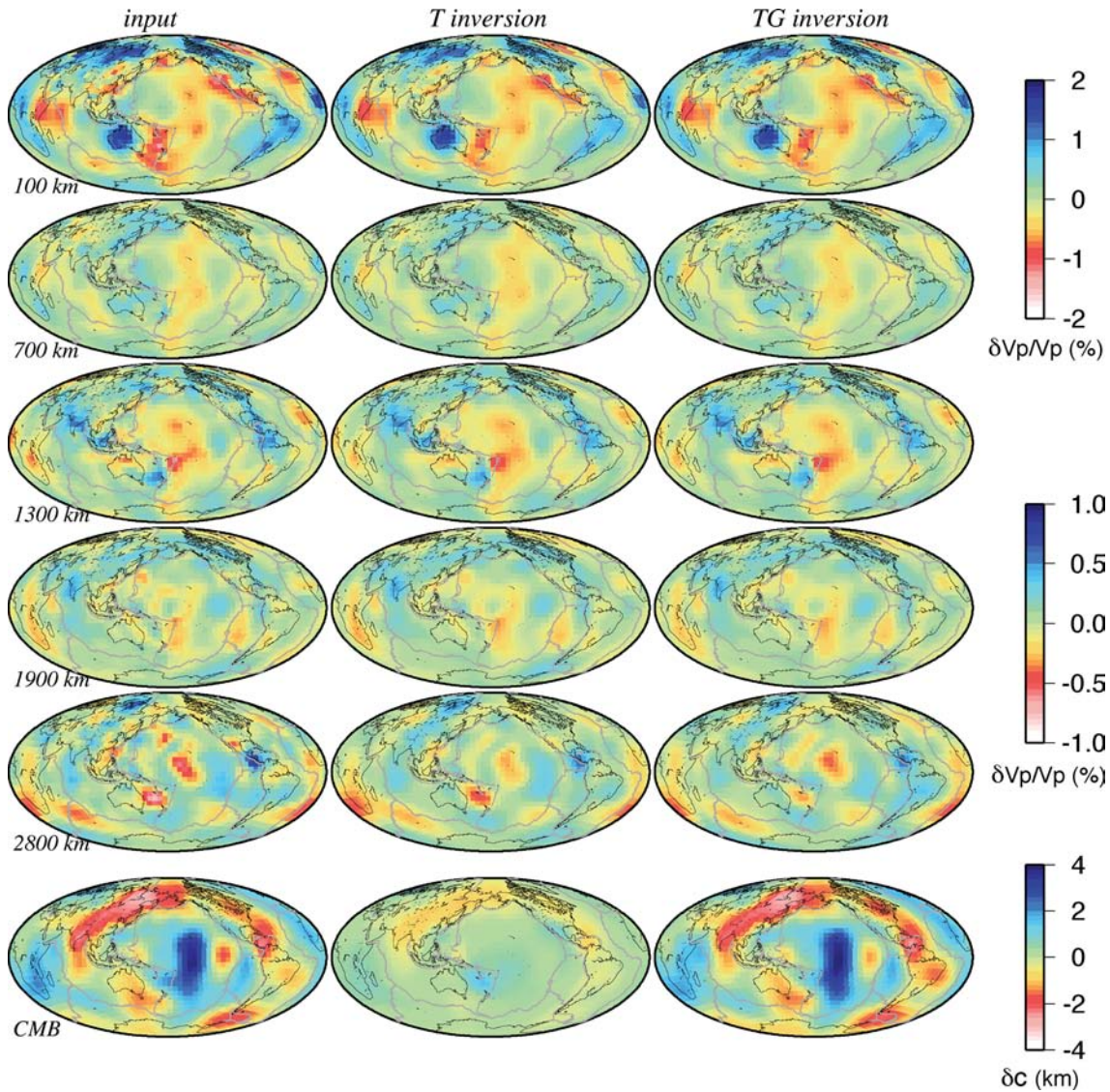


**Figure 7.** Same, with output models obtained inverting  $P+PKP_{df}$  data. All models include mantle velocity heterogeneities (per cent) and CMB topography (km).

**Table 3.** Recovery test: rms of the difference between input and output models (acronyms same as Table 1) for a realistic mantle  $v_p$  structure.

Inverted data	MAN	LMM	CMB
$P + PcP (T)$	0.056	0.0744	0.895
$P + PcP (TG)$	0.058	0.065	0.151
$P + PKP (T)$	0.0549	0.0737	0.884
$P + PKP (TG)$	0.057	0.098	0.218

**Table 4.** Recovery test: correlation between input and output models (acronyms same as Table 1) for a realistic mantle  $v_p$  structure.

Inverted data	MAN	LMM	CMB
$P + PcP (T)$	0.980	0.934	0.677
$P + PcP (TG)$	0.979	0.943	0.991
$P + PKP (T)$	0.980	0.922	0.817
$P + PKP (TG)$	0.978	0.874	0.984

times lower than in the immediately overlying layer (Fig. 1). The resulting kernels are shown in Fig. 2 and were discussed in Section 2.1. We show in Fig. 14  $TG$  models based on the kernels of Fig. 2. Even in the lowermost mantle, mapped  $v_p$  is only marginally perturbed with respect to the  $TG$  models of Section 5.1. CMB undulations, on the other hand, change significantly, with a similar pattern but amplitude reduced by over 75 per cent. In addition, the localized depression to the west of Cocos plate fades away almost completely.

Variance reduction of seismic data achieved by the  $TG$  models of this section is only marginally different from those illustrated in Section 5.1 ( $\sim 1$  per cent difference depending on the phase, with the  $PcP$  variance reduction slightly higher for the low-viscosity models, and that of other data sets slightly lower). Interestingly, however, the low-viscosity models are characterized by mapped CMB ellipticity systematically closer to the value given by, for example, Gwinn *et al.* (1986) based on independent geodetic observations, as discussed in Section 5.4 later.

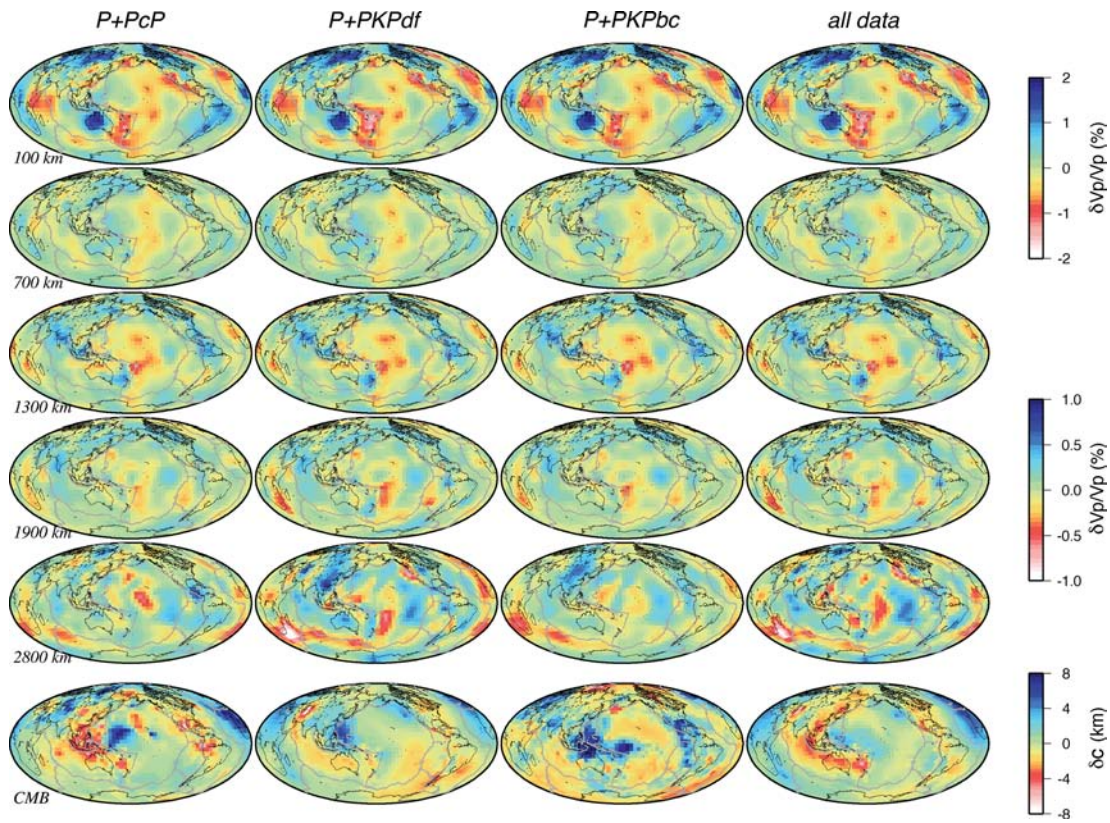


**Figure 8.** Seismic images of the Earth's mantle (rows 1 to 5) (per cent) and CMB topography (last row) (km) obtained from the joint direct  $P$  and  $PcP$  data set (first column), joint  $P$  and  $P+PKPdf$  (second column), joint  $P$  and  $PKPbc$  (third column) and entire  $P$ ,  $PcP$ ,  $PKP$  data set (fourth column). The maps refer to purely tomographic inversion of ISC data.

#### 5.4 Excess ellipticity of the CMB

The shift of the period of the Earth's free core nutation predicted using hydrostatic theory from the one observed using VLBI geodesy has been interpreted as due to excess CMB ellipticity caused by convection (Forte *et al.* 1995), with a peak-to-valley deviation of  $490 \pm 110$  m (Gwinn *et al.* 1986). Table 5 shows the values we find depending on data and method ( $T/TG$ ): for each of our CMB topography models we compute a spherical harmonic expansion, filter out all components but the  $l = 2$ ,  $m = 0$  one, and measure the peak to valley deviation of the resulting map.  $T$  models are overall closer to the VLBI-observed CMB ellipticity than  $TG$ . If we use a more realistic rheology, including a post-perovskite layer modelled as a very low viscosity region at the base of the mantle, our  $TG$  models agree slightly better with the observations of Gwinn *et al.* (1986).

To rule out the possibility of trade-off between the choice of the viscosity profile and that of the density-to-velocity conversion factor, we test the effect of reducing by 1000 times the value of  $\delta \ln \rho / \delta \ln v_p$  (instead of that of the radial viscosity) in the lowermost 250 km of the mantle. Such reduction in  $\delta \ln \rho / \delta \ln v_p$  could be expected based on the indication, from mineral physics, that velocity–density scaling could decrease with increasing pressure. We find, again, values of CMB ellipticity too high (peak to valley anomaly of 1 km) to be consistent with the VLBI data; at this stage, a low-viscosity post-perovskite layer in the  $TG$  approach remains the only mechanism to explain better VLBI-observed CMB ellipticity.

#### 6 DISCUSSION

We have constructed a series of tomographic models of mantle  $P$ -wave velocity and CMB topography accounting for the mechanical coupling between mantle heterogeneity which drives viscous flow, and fluid outer core, whose upper boundary is deformed accordingly. Instead of inverting seismic traveltimes for both mantle structure and CMB deflections, as it has been done so far, the new models are built with mantle heterogeneity as the only unknown of our inverse problem, but taking into account topography seen by the data at the CMB. We thus get mantle–CMB models that are both geodynamically sound and consistent with seismic data. The same concept can in principle be applied to other mantle discontinuities. Including this mantle–CMB geodynamic coupling is practically equivalent to a physically based regularization of the inverse problem.

Our approach rests on the assumption that the chemical contribution to mantle heterogeneity be negligible compared to the thermal one. More work (for example, combining the database used here with  $S$ -wave observations) will be needed to take proper account of compositional heterogeneity (e.g. Karato 2003; Deschamps & Trampert 2003; Trampert *et al.* 2004; Della Mora *et al.* 2011), though there are indications that thermal effects might still be predominant (Forte & Mitrović 2001; Simmons *et al.* 2009). Our results, particularly the response of CMB topography to mantle density perturbations, also depend on the radial viscosity profile of the mantle, notoriously difficult to constrain particularly at large depths (Soldati *et al.* 2009); however, repeating our calculations with a set of quite different viscosity profiles (Fig. 1) we have found that at

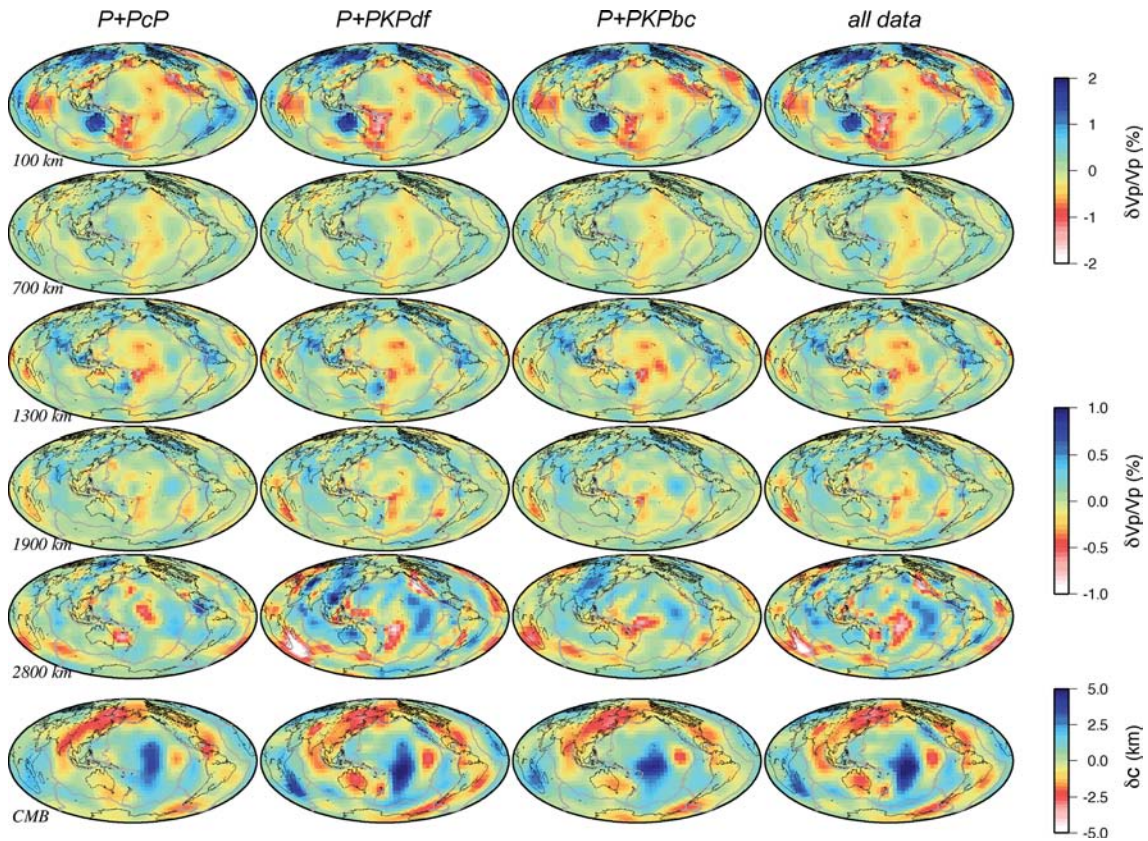


**Figure 9.** Maps of mantle  $v_p$  anomalies ( per cent) and CMB topography (km). The maps should be read as in the previous figure. They are derived through a tomographic-geodynamic (TG) inversion.

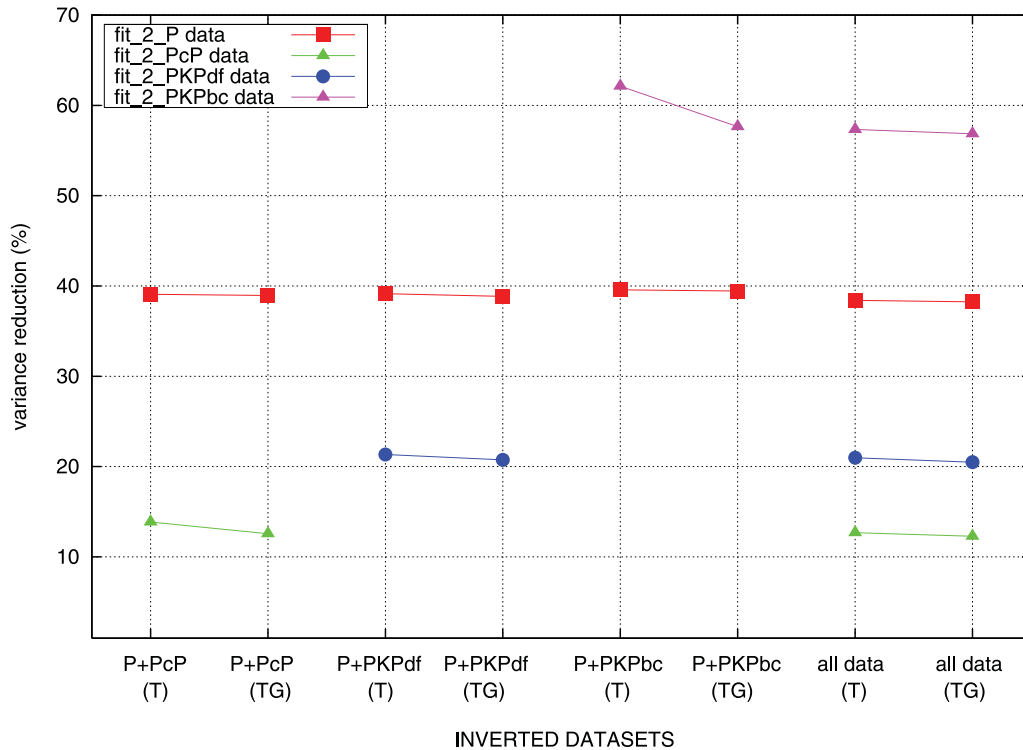


**Figure 10.** Weighted variance reduction (weighting used in inversion) achieved by  $T$  and  $TG$  models, based on the combined  $P$  and  $PcP$ ,  $P$  and  $PKPdf, bc$ , and complete databases: each datapoint on the horizontal axis corresponds to a different  $T$  or  $TG$  model, obtained from a different data set, as indicated. For each model, we compute the variance reduction of the data set associated with each phase (four values on the vertical axis), that is,  $P$  (red squares),  $PcP$  (green triangles),  $PKPdf$  (blue circles),  $PKPbc$  (purple triangles).

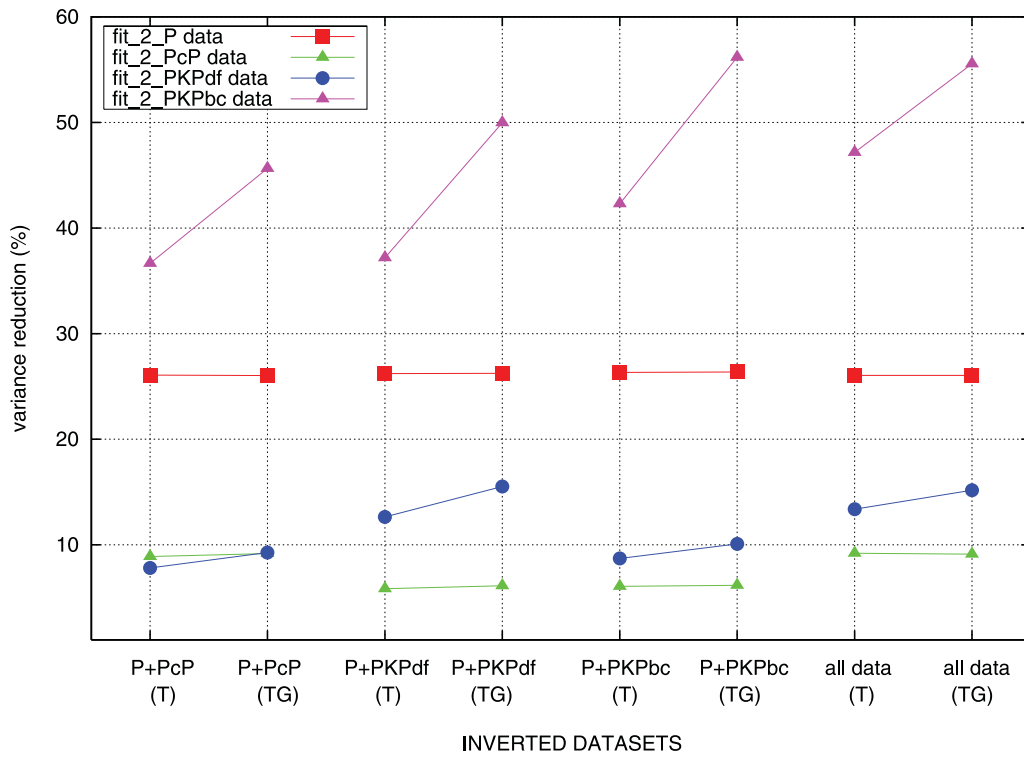


Figure 11. Same as Fig. 10, but variance reduction is computed without weighting the data.

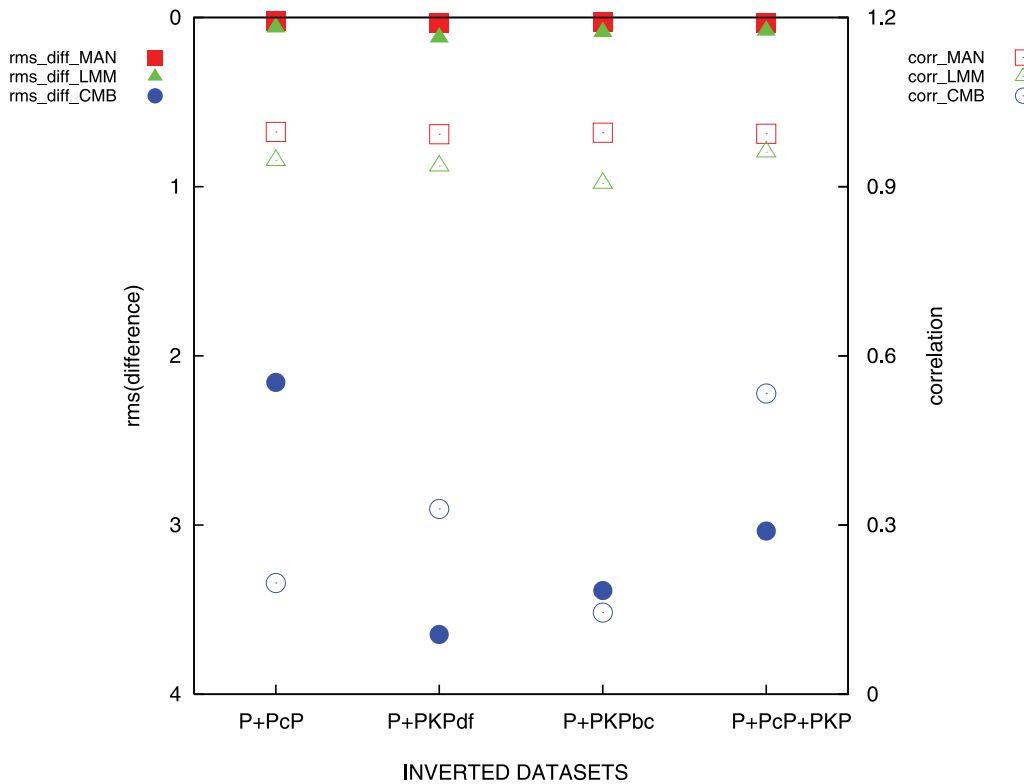
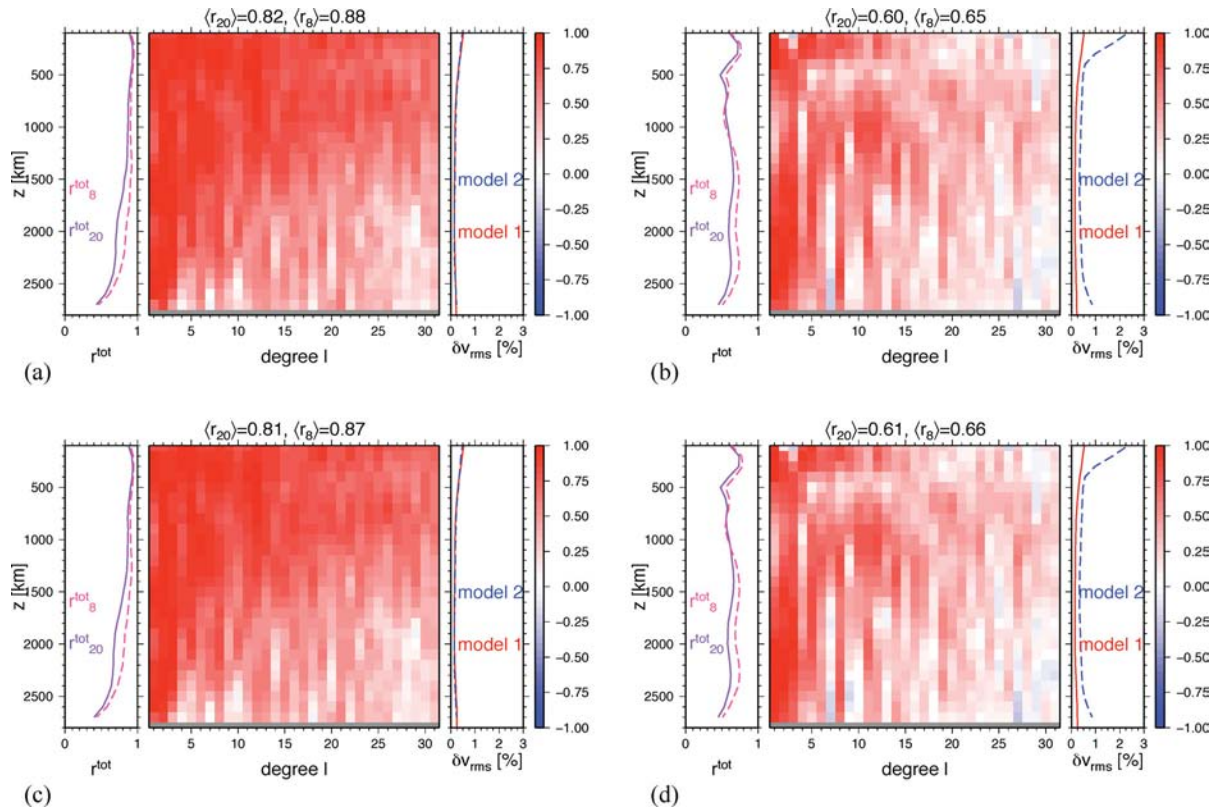


Figure 12. Similarity between *T* and *TG* models by means of their rms difference and correlation computed considering the whole mantle (red), the lowermost mantle (green) and the CMB alone (blue).

least the overall pattern (if not amplitude) of mapped CMB topography remains stable. In addition, since independent data are available to test the quality of our CMB maps (e.g. waveforms of diffracted seismic phases; eigenfrequency splitting of CMB-sensitive modes),

in future work it might be possible to use the latter to evaluate the reliability of proposed viscosity models. A final assumption of our calculations is that the outer core be laterally homogenous. This is occasionally questioned, and there is emerging evidence of radial



**Figure 13.** (a) (Left plot) correlation  $r_8$  up to harmonic degree 8, and  $r_{20}$  up to harmonic degree 20, as functions of depth between our  $T$  model and the  $v_P$  model  $PMEAN$  of Becker & Boschi (2002); (middle plot) correlation between the same two models as a function of depth, and harmonic degree; (right plot) rms of both models as a function of depth, with our model marked as model 1 and  $PMEAN$  as model 2. (b) same as (a), but for our  $T$  model and the  $v_S$  model  $SMEAN$  of Becker & Boschi (2002). (c)  $TG$  and  $PMEAN$ . (d)  $TG$  and  $SMEAN$ .

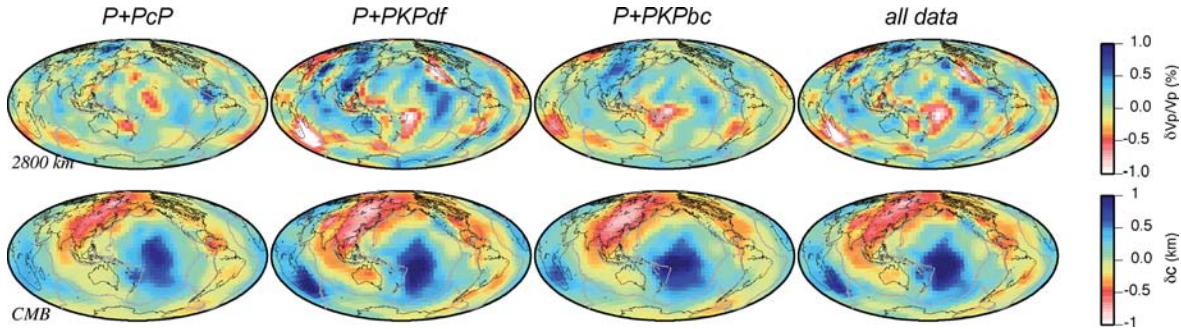


**Figure 14.**  $TG$  maps of  $\delta v_P/v_P$  (per cent) in the lowermost mantle (depth = 2700–2900 km) obtained using a viscosity profile for the mantle, which mimics the presence of the perovskite–postperovskite phase transition. Bottom plots refer to the corresponding CMB topography (km) computed geodynamically from mantle  $v_P$  models. The models were obtained inverting different subsets of the data, left to right, as indicated.

**Table 5.** Predicted excess CMB ellipticity (km) obtained from models  $T$  (Fig. 8) and  $TG$  (Figs 9, 14),  $TG$  (ppv) with a low-viscosity post-perovskite layer (Section 5.3), and  $TG$  ( $\delta \ln \rho / \delta \ln v_P$ ).

Inverted data	$T$ model	$TG$ model	$TG$ model (ppv)	$TG$ model ( $\delta \ln \rho / \delta \ln v_P$ )
$P + PcP$	0.948	1.221	0.360	1.225
$P + PKPdf$	0.490	0.956	0.295	0.98
$P + PKPbc$	2.172	1.270	0.390	1.302
<i>all data</i>	0.390	1.029	0.308	1.046

compositional variation in the outermost outer core (e.g. Helffrich & Kaneshima 2010), but preliminary experiments not shown here for brevity show that our  $TG$  maps are not strongly perturbed by the

introduction of outer-core heterogeneity (S. Della Mora *et al.*, in preparation).

The new joint tomographic–geodynamic models (labelled  $TG$ ) are compared to models ( $T$ ) obtained via a classic tomographic treatment (e.g. Boschi & Dziewonski 2000; Forte & Mitrovica 2001) through a series of inversions of synthetic and real data. From the checkerboard and recovery tests of Section 4 it emerges that while  $T$  and  $TG$  methods perform equally well in reproducing the input mantle model, the latter approach enhances the resolution of the CMB input topography.

Because the CMB topography is not directly inverted for, the  $TG$  approach involves a much smaller number of free parameters; nevertheless, we find that our new  $TG$  models explain the database of Antolik *et al.* (2001) at least as well as the  $T$  ones. This can be

interpreted as an indication that mantle flow is predominantly governed by thermal, rather than compositional, heterogeneity. On the other hand, the amplitude of the  $P$ -wave velocity anomalies in our  $TG$  models of the lowermost mantle remains basically unchanged compared to that of  $T$  models, and so does the ratio  $\delta v_S/\delta v_P$ , confirming that a certain degree of compositional heterogeneity exists in this depth range (Simmons *et al.* 2010; Della Mora *et al.* 2011).

The CMB maps obtained on the basis of  $PcP$  versus  $PKP$  data are highly correlated, as opposed to the systematic discrepancy found by classic tomographic approaches (Rodgers & Wahr 1993; Boschi & Dziewonski 2000; Soldati *et al.* 2003). Robust structure that emerged from earlier purely tomographic inversion at least of  $PcP$  data is confirmed by our  $T$  and  $TG$  inversions here. In particular, the spherical-harmonic degree-2 character of  $TG$  maps of the CMB (bottom panels of Fig. 9), depressed under the Pacific rim (corresponding to possible sinking slabs) and relatively elevated under the Pacific and African superplumes, is very similar to what is found in classical tomography, both here (Fig. 8, bottom left and bottom right panels) and in earlier studies (e.g. Morelli & Dziewonski 1987; Rodgers & Wahr 1993; Soldati *et al.* 2003). In addition, our  $TG$  models are found to reduce the variance of normal-mode eigenfrequency splitting observations (Koelemeijer & Deuss, personal communication, 2011). These are all strong indications that the data have at least some useful sensitivity to CMB topography.

The  $TG$  approach introduced here reduces the amplitudes of CMB topography by about 30 per cent, which is consistent with geodynamic results found in the literature (e.g. Forte *et al.* 1995). The peak-to-valley deviation of the  $l = 2$ ,  $m = 0$  component of CMB inferred from VLBI observations is more difficult to match, but can be reproduced (although with reasonable error) provided that a more realistic rheology is employed: namely, a 250 km thick low viscosity layer above the CMB simulating the presence of post-perovskite.

## ACKNOWLEDGMENTS

This study benefitted from the insightful comments of Andrea Morelli, Sebastian Rost and one anonymous reviewer. Paula Koelemeijer provided important feedback regarding our models' capability to explain normal-mode data. LB wishes to thank Domenico Giardini for his constant support and encouragement.

## REFERENCES

- Ammann, M.W., Brodholt, J.P., Wookey, J. & Dobson, D.P., 2010. First-principles constraints on diffusion in lower-mantle minerals and a weak  $D'$  layer, *Nature*, **465**(7297), 462–465.
- Antolik, M., Ekström, G. & Dziewonski, A.M., 2001. Global event location with full and sparse data sets using three-dimensional models of mantle  $P$ -wave velocity, *Pure appl. Geophys.*, **158**(1–2), 291–317.
- Becker, T.W. & Boschi, L., 2002. A comparison of tomographic and geodynamic mantle models, *Geochem. Geophys. Geosyst.*, **3**, 1003, doi:10.1029/2001GC000168.
- Boschi, L., 2003. Measures of resolution in global body wave tomography, *Geophys. Res. Lett.*, **30**(19), doi:10.1029/2003GL018222.
- Boschi, L. & Dziewonski, A.M., 1999. High- and low-resolution images of the Earth's mantle: implications of different approaches to tomographic modeling, *J. geophys. Res.*, **104**(B11), 25 567–25 594.
- Boschi, L. & Dziewonski, A.M., 2000. Whole Earth tomography from delay times of  $P$ ,  $PcP$ , and  $PKP$  phases: lateral heterogeneities in the outer core or radial anisotropy in the mantle?, *J. geophys. Res.*, **105**(B6), 13 675–13 696.
- Boschi, L., Ampuero, J.P., Peter, D., Mai, P.M., Soldati, G. & Giardini, D., 2007. Petascale computing and resolution in global seismic tomography, *Phys. Earth. planet. Inter.*, **163**(1–4), 245–250.
- Boschi, L., Becker, T.W. & Steinberger, B., 2008. On the statistical significance of correlations between synthetic mantle plumes and tomographic models, *Phys. Earth. planet. Inter.*, **167**(3–4), 230–238.
- Buffett, B.A., Mathews, P.M. & Herring, T.A., 2002. Modeling of nutation and precession: effects of electromagnetic coupling, *J. geophys. Res.*, **107**(B4), doi:10.1029/2001JB000390.
- Della Mora, S., Boschi, L., Tackley, P.J., Nakagawa, T. & Giardini, D., 2011. Low seismic resolution cannot explain S/P velocity decorrelation in the lower mantle, *Geophys. Res. Lett.*, **38**, L12303, doi:10.1029/2011GL047559.
- Deschamps, F. & Trampert, J., 2003. Mantle tomography and its relation to temperature and composition, *Phys. Earth planet. Inter.*, **140**(4), 277–291.
- Dziewonski, A.M. & Anderson, D.L., 1981. Preliminary reference earth model, *Phys. Earth. planet. Inter.*, **25**(4), 297–356.
- Dziewonski, A.M. & Gilbert, F., 1976. Effect of small, aspherical perturbations on travel times and a re-examination of corrections for ellipticity, *Geophys. J. R. astr. Soc.*, **44**(1), 7–17.
- Engdahl, E.R., van der Hilst, R. & Buland, R., 1998. Global teleseismic earthquake relocation with improved travel times and procedures for depth determination, *Bull. seism. Soc. Am.*, **88**(3), 722–743.
- Forte, A.M. & Mitrovica, J.X., 2001. Deep-mantle high-viscosity flow and thermochemical structure inferred from seismic and geodynamic data, *Nature*, **410**(6832), 1049–1056.
- Forte, A.M. & Peltier, W.L., 1991. Viscous-flow models of global geophysical observables 1: forward problems, *J. geophys. Res.*, **96**, 20 131–20 159.
- Forte, A.M., Woodward, R.L. & Dziewonski, A.M., 1994. Joint inversions of seismic and geodynamic data for models of 3-dimensional mantle heterogeneity, *J. geophys. Res.*, **99**, 21 857–21 877.
- Forte, A.M., Mitrovica, J.X. & Woodward, R.L., 1995. Seismic-geodynamic determination of the origin of excess ellipticity of the core–mantle boundary, *Geophys. Res. Lett.*, **22**(9), 1013–1016.
- Gwinn, C.R., Herring, T.A. & Shapiro, I.I., 1986. Geodesy by radio interferometry: studies of the forced nutations of the Earth 2. Interpretation, *J. Geophys. Res.*, **91**(B5), 4755–4765.
- Hager, B.H., Clayton, R.W., Dziewonski, A.M., Richards, M.A. & Comer, R.P., 1985.  $P$  and  $PcP$  travel time tomography for the core–mantle boundary, *Nature*, **313**, 541–545.
- Helfrich, G. & Kaneshima, S., 2010. Outer-core compositional stratification from observed core wave speed profiles, *Nature*, **468**, doi:10.1038/nature09636.
- Ishii, M. & Tromp, J., 1999. Normal-mode and free-air gravity constraints on lateral variations in velocity and density of Earth's mantle, *Science*, **285**(5431), 1231–1236.
- Karato, S. I., 1993. Importance of anelasticity in the interpretation of seismic tomography, *Geophys. Res. Lett.*, **20**, 1623–1626.
- Karato, S.I., 2003, *The Dynamic Structure of the Deep Earth*, Princeton University Press, Princeton, PA.
- Karato, S.I. & Karki, B.B., 2001. Origin of lateral variation of seismic wave velocities and density in the deep mantle, *J. geophys. Res.*, **106**(B10), 21 771–21 783.
- Lassak, T.M., McNamara, A.K. & Zhong, S., 2007. Influence of thermochemical piles on topography at Earth's core–mantle boundary, *Earth planet. Sci. Lett.*, **261**(3–4), 443–455.
- Lassak, T.M., McNamara, A.K., Garnero, E.J. & Zhong, S.J., 2010. Core–mantle boundary topography as a possible constraint on lower mantle chemistry and dynamics, *Earth planet. Sci. Lett.*, **289**(1–2), 232–241.
- Menke, W., 1989, *Geophysical Data Analysis: Discrete Inverse Theory (revised edition)*, Academic Press, San Diego, CA.
- Mitrovica, J. & Forte, A.M., 1997. The radial profile of mantle viscosity: results from the joint inversion of convection and post-glacial rebound observables, *J. geophys. Res.*, **102**, 2751–2769.
- Mooney, W.D., Laske, G. & Masters, T.G., 1998. Crust 5.1: A global crustal model at 5 degrees x 5 degrees, *J. geophys. Res.*, **103**(B1), 727–747.
- Morelli, A. & Dziewonski, A.M., 1987. Topography of the core–mantle boundary and lateral homogeneity of the liquid core, *Nature*, **325**, 678–683.
- Moucha, R., Forte, A.M., Mitrovica, J.X. & Daradich, A., 2007. Lateral variations in mantle rheology: implications for convection related

- surface observables and inferred viscosity models, *Geophys. J. Int.*, **169**(1), 113–135.
- Murakami, M., Hirose, K., Kawamura, K., Sata, N. & Ohishi, Y., 2004. Post-perovskite phase transition in MgSiO<sub>3</sub>, *Science*, **304**, doi:10.1126/science.1095932.
- Obayashi, M. & Fukao, Y., 1997. P and PcP travel time tomography for the core-mantle boundary, *J. geophys. Res.*, **102**, 17 825–17 841.
- Oganov, A.R. & Ono, S., 2004. Theoretical and experimental evidence for a post-perovskite phase of MgSiO<sub>3</sub> in Earth's D'' layer, *Nature*, **430**, 445–448.
- Piersanti, A., Boschi, L. & Dziewonski, A.M., 2001. Estimating lateral structure in the Earth's outer core, *Geophys. Res. Lett.*, **28**(8), 1659–1662.
- Qin, Y.L., Capdeville, Y., Maupin, V., Montagner, J.P., Lebedev, S. & Beucler, E., 2008. SPICE benchmark for global tomographic methods, *Geophys. J. Int.*, **175**(2), 598–616.
- Ritsema, J., Heijst, H.J.V. & Woodhouse, J.H., 1999. Complex shear wave velocity structure imaged beneath Africa and iceland, *Science*, **286**(5446), 1925–1928.
- Ritsema, J., Heijst, H.J.V. & Woodhouse, J.H., 2004. Global transition zone tomography, *J. geophys. Res.*, **109**(B2), B02302, doi:10.1029/2003JB002610.
- Ritzwoller, M., Masters, G. & Gilbert, F., 1986. Observations of anomalous splitting and their interpretation in terms of aspherical structure, *J. geophys. Res.*, **91**(B10), 203–228.
- Rodgers, A. & Wahr, J., 1993. Inference of core-mantle boundary topography from ISC PcP and PKP traveltimes, *Geophys. J. Int.*, **115**, 991–1011.
- Schuberth, B.S.A., Bunge, H.P., Steinle-Neumann, G., Moder, C. & Oeser, J., 2009. Thermal versus elastic heterogeneity in high-resolution mantle circulation models with pyrolite composition: high plume excess temperatures in the lowermost mantle, *Geochem. Geophys. Geosyst.*, **10**, Q01W01, doi:10.1029/2009GC002401.
- Simmons, N.A., Forte, A.M. & Grand, S.P., 2009. Joint seismic, geodynamic and mineral physical constraints on three-dimensional mantle heterogeneity: implications for the relative importance of thermal versus compositional heterogeneity, *Geophys. J. Int.*, **177**(3), 1284–1304.
- Simmons, N.A., Forte, A.M., Boschi, L. & Grand, S.P., 2010. GyPSuM: a joint tomographic model of mantle density and seismic wave speeds, *J. geophys. Res.*, **115**, B12310, doi:10.1029/2010JB007631.
- Soldati, G. & Boschi, L., 2005. The resolution of whole Earth seismic tomographic models, *Geophys. J. Int.*, **161**(1), 143–153.
- Soldati, G., Boschi, L. & Piersanti, A., 2003. Outer core density heterogeneity and the discrepancy between PKP and PcP travel time observations, *Geophys. Res. Lett.*, **30**(4), doi:10.1029/2002GL016647.
- Soldati, G., Boschi, L., Deschamps, F. & Giardini, D., 2009. Inferring radial models of mantle viscosity from gravity (GRACE) data and an evolutionary algorithm, *Phys. Earth. planet. Int.*, **176**(1–2), 19–32.
- Steinberger, B. & Antretter, M., 2006. Conduit diameter and buoyant rising speed of mantle plumes: implications for the motion of hot spots and shape of plume conduits, *Geochem. Geophys. Geosyst.*, **7**, doi:10.1029/2006GC001409.
- Su, W.J. & Dziewonski, A.M., 1995. Inner-core anisotropy in 3 dimensions, *J. geophys. Res.*, **100**(B6), 9831–9852.
- Tarantola, A., 2005. *Inverse Problem Theory*, SIAM, Philadelphia, PA.
- Tosi, N., Cadek, O., Martinec, Z., Yuen, D.A. & Kaufmann, G., 2009. Is the long-wavelength geoid sensitive to the presence of postperovskite above the core-mantle boundary?, *Geophys. Res. Lett.*, **36**, L05303, doi:10.1029/2008GL036902.
- Trampert, J., Deschamps, F., Resovsky, J. & Yuen, D., 2004. Probabilistic tomography maps chemical heterogeneities throughout the lower mantle, *Science*, **306**(5697), 853–856.
- Yamazaki, D., Yoshino, T., Ohfuji, H., Ando, J.I. & Yoneda, A., 2006. Origin of seismic anisotropy in the D'' layer inferred from shear deformation experiments on post-perovskite phase, *Earth planet. Sci. Lett.*, **252**(3–4), 372–378.